universität wien

MASTERARBEIT / MASTER'S THESIS

Titel der Masterarbeit / Title of the Master's Thesis

„Effects of the disk's gravitational potential on the structure and long-term evolution of protoplanetary disks“

verfasst von / submitted by

Lukas Gehrig, BSc

angestrebter akademischer Grad / in partial fulfilment of the requirements for the degree of

Master of Science (MSc)

Wien, 2020 / Vienna, 2020

Studienkennzahl lt. Studienblatt / degree programme code as it appears on the student record sheet:	A 066861
Studienrichtung lt. Studienblatt / degree programme as it appears on the student record sheet:	Masterstudium Astronomie
Betreut von / Supervisor:	ao. Univ.-Prof. Dr. Ernst Dorfi

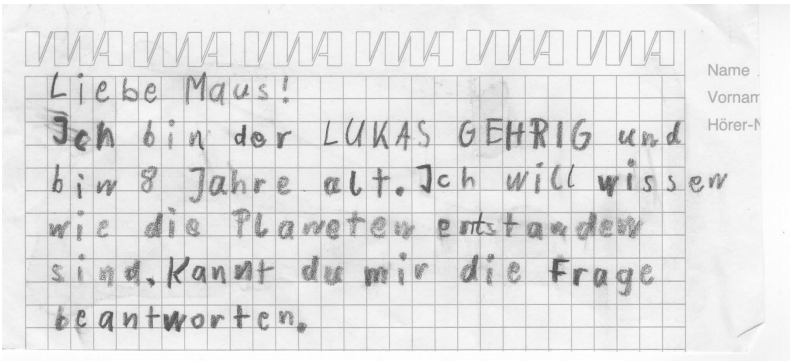
Liebe Maus!
Ich bin der LUKAS GEHRIG und
bin 8 Jahre alt. Ich will wissen
wie die Planeten entstanden
sind. Kannt du mir die Frage
beantworten.

*Eigentlich wollte ich von diesen vorangestellten Dingen absehen, aber ich werde dazu gezwungen.

Zusammenfassung

Kontext. Protoplanetare Scheiben gelten als mögliche Lösung des Drehimpulsproblems und werden meist mittels expliziter, numerischer Verfahren simuliert. Für diese expliziten Verfahren gelten jedoch spezielle Einschränkungen. Daher verspricht die implizite Berechnung protoplanetarer Scheiben auf einem adaptiven Gitter, neue Erkenntnisse in der Struktur und Evolution der Scheiben zu liefern. Der TAPIR-code löst die Gleichungen der Radiation-Hydrodynamic (RHD), unter der Annahme einer vernachlässigbaren Scheibenmasse. Daher hat das gravitative Potential der Scheibe keinen Einfluss auf ihre Struktur und ihre zeitliche Entwicklung.

Ziele. Ziel dieser Arbeit ist es, den Einfluss der Scheibenmasse zu dem bestehenden Model hinzuzufügen, indem das gravitative Eigenpotenzial einer dünnen Scheibe für eine beliebige Dichteverteilung in des bestehende Model implementiert wird. In weiterer Folge soll die Auswirkung des Eigenpotenzials auf die Scheibe untersucht werden.

Methoden. Ausgehend von der allgemeinen Lösung der Poisson-Gleichung, wird das Potenzial in radialer Richtung unter der Annahme einer dünnen, symmetrischen Scheibe mittels kompletter elliptischer Integrale beschrieben. Dank der Finiten Volumens Methode lässt sich das Potenzial sowie dessen Gradient in eine Summe umschreiben, die numerisch leicht zu berechnen ist. In vertikaler Richtung wird der Einfluss des Potenzials auf die Skalenhöhe beschrieben. Ein Vergleich der gravitativen Beschleunigung des Sterns und der Scheibe liefert schließlich ein Kriterium Q_{SG}, das veranschaulichen soll, ab wann der Einfluss der Eigengravitation der Scheibe zu berücksichtigen ist.

Ergebnisse. Das resultierende Potenzial kann sowohl durch die Berechnung der Gravitationsenergie, überprüfen der Massenerhaltung sowie weitere Tests verifiziert werden. Anschließend werden für verschiedene Werte von Q_{SG} die Scheibenstruktur und die zeitliche Entwicklung, mit und ohne Eigenpotenzial, verglichen.

Schlussfolgerung. Die Ergebnisse legen nahe, dass für schwerer werdende Scheiben die Scheibengravitation eine immer größere Rolle spielt. Erhöht sich die Masse einer Scheibe bis zu dem Punkt, an dem der Wert von Q_{SG} in einem Bereich der Scheibe unter 1 liegt, lassen sich erhebliche Unterschiede in der Struktur und der zeitlichen Entwicklung der Scheibe feststellen. Für eine geringe Scheibenmasse und somit einem hohen Q_{SG}, kann die Scheibengravitation vernachlässigt werden.

Abstract

Context. Protoplanetary disks are a possible solution to the angular momentum problem and are primarily simulated using explicit numerical methods, which are subjected to certain restrictions. The implicit calculation of thin protoplanetary disks on an adaptive grid however, promises to provide new insights in disk structure and long-term evolution. The TAPIR code solves the equations of radiation hydrodynamics (RHD), assuming a negligible disk-mass. Thus, the disk's gravitational potential has no influence on the structure and evolution of the disk itself.

Aims. The aim of this work is to study the influence of the disk's gravitational potential by implementing additional equations into the present model.

Methods. Starting from the basic solution of the Poisson equation, the potential of the disk is calculated under the assumption of a thin, symmetrical disk using complete elliptical integrals. Due to the finite volume method, the potential as well as its gradient in radial direction can be casted into a sum which can be implemented into the present model. In vertical direction the potential is considered as an additional factor for the pressure scale height. Comparing the gravitational acceleration of the star and the disk leads to a criterion Q_{SG}, which describes the importance of the disk's gravity.

Results. The resulting potential can be verified by e.g. calculating the gravitational energy, the conservation of mass and with other tests. The influence of the disk's self gravity on the structure and evolution of the disk is examined by varying Q_{SG}.

Conclusion. The results show that for higher disk-masses the influence of the disk's self gravity increases. If the disk mass increases to the point, where the value of Q_{SG} falls below 1 within the disk, significant differences in disk structure and evolution are ascertain. For low mass disks (high Q_{SG}), the influence of the disk's self gravity is negligible.

Contents

1 Introduction

During the collapse of a interstellar cloud towards a protostar, angular momentum has to be reduced to overcome the angular momentum problem (e.g. [32]). One possibility to decrease angular momentum is the formation of a protoplanetary accretion disk, which transports the angular momentum outwards by turbulence, while mass is accreted towards the central star (e.g. [4] or [38]). According to e.g. [4], the structure of a protoplanetary disk can be considered as thin in vertical direction, while maintaining Keplerian velocity in angular direction. The radial extend $r_{\mathrm{in}} < 0.1\,\mathrm{AU} < r < 100\,\mathrm{AU} < r_{\mathrm{out}}$ is estimated e.g. by reproducing episodic accretion events (for the inner radius r_{in} e.g. [6] or [9]) or by observations (for the outer radius r_{out}, e.g. [3]). The radii close to the central star entail a small dynamic (orbital) timescale τ_{K} at the inner boundary of the disk ($\tau_{\mathrm{K}} \sim$ days) whereas the total lifetime of a disk can range up to 10 Myr [26].

The simulation of a protoplanetary disk is often executed with explicit numerical methods (e.g. [40] or [46]), which are restricted e.g. by the so-called Courant, Friedrichs and Lewy (CFL) condition [14]. During an explicit simulation, the smallest timescale limits the timestep. Especially, the inner regions of the disk are restricted, due to the small dynamic timescale and so, the whole radial range of a disk is not possible to be covered with these simulations over the whole lifetime. Implicit numeric methods are not bound to the timestep limitation (e.g. [15]) and are able to deal with the whole lifetime of the disk, including also the inner regions, which (according to e.g. [46] or [38]) are important for the structure and evolution of the disks. The TAPIR code (presented in [38]) is able to simulate protoplanetary disks, assuming axial-symmetry and an isothermal disk-structure in vertical direction. The TAPIR code however, is still under development and one physical aspect, not yet considered, is the disk-mass (assumed to be negligible compared to the stellar mass) and the influence of the resulting gravitational potential on the structure and long-term evolution of the disk. Although the disk's potential is small compared to the potential of the central object, mass transport in the disk leads to small local changes, where their effect on the evolution of the disk remains uncertain.

In this work, the influence of the gravitational potential of the protoplanetary disk on both, the structure and the long-term evolution of the disk is examined. The first chapter will outline some basic assumptions the code is based upon as well as the scales of the physical system it represents. The equations, physical assumptions

and the discretization scheme are described in the second chapter, followed by the numerical features e.g. the adaptive grid equation and the choice of the boundary conditions. These first chapters shall combine the most important equations and assumptions, in both physical and numerical manner, the code is based upon and serve as an overview for using the code, in particular for disks. For deeper insights or exact derivations the respective references are given. In the fourth chapter the gravitational potential of the protostellar disk as well as its gradient in radial and vertical direction are derived and the implementation into the code is shown. To determine, whether the gravitational potential of the disk noticeably influences the disk's structure and long-term evolution, a criterion Q_{SG} is formulated. The implementation is afterwards tested for correctness, followed by simulations showing the effect of the disk's gravity for different values of Q_{SG}.

1.1 TAPIR Code

The evolution of protoplanetary disks can be simulated by the TAPIR (The AdaPtive Implicit RHD) code, which has been described by [15] and [38]. This code is designed to produce a viscous, steady state initial model of a protoplanetary disk and calculate the temporal evolution of the disk, by utilizing an implicit scheme based on that model in $1+1$ dimensions. Five primary variables are taken into account: the surface density Σ, the radial velocity component u_r, the angular velocity component u_φ, the internal energy e as well as the location of the radial gridpoint r, with the help of an adaptive grid (see [16]).

1.2 Basic Assumptions and Key Numerical Aspects

Before describing the code's physics in particular, some basic assumptions have to be made [38]. First of all, the coordinates are based on a cylindrical coordinate system $\mathbf{x} = x(r, \varphi, z)$. Additionally, cylindrical symmetry is assumed and thus all φ dependencies can be neglected. Another key assumption is the hydrostatic equilibrium in z direction. No vertical velocity is allowed and furthermore, no changes in z direction are allowed for the velocities in r and φ direction. The velocity reduces to a time and radius dependent quantity $\mathbf{u} = (u_r(r,t), u_\varphi(r,t), 0)$. The internal energy also remains constant (isothermal) in z resulting in a constant speed of sound c_s at a given radius [38]. Finally, a thin disk approximation $z \ll r$ is used (e.g. [4]) which results i.e. in

$$\frac{1}{(r^2+z^2)^{\frac{3}{2}}} \approx \frac{1}{r^3}. \tag{1.1}$$

Together with the independence of the angular coordinate φ, vertically integrated quantities can be used. The density ρ converts i.e. into a surface density Σ (see e.g. [4] or [37]) according to

$$\Sigma(r,t) = \int_{-\infty}^{\infty} \rho(r,z,t)\, dz\,. \tag{1.2}$$

The following numerical features are characteristic for the TAPIR code. They are listed here as an overview and are specified in the following sub-chapters. First of all, the code is using an implicit scheme and is therefore not bound to the Courant, Friedrichs and Lewy (CFL) condition [14] with the timestep δt and the radial orbital distance Δx

$$\delta t \leq \frac{\Delta x}{|\mathbf{u}| + c_s}\,. \tag{1.3}$$

Especially for large velocities and close orbits, this restriction is impairing. According to [38], these inner regions are especially important for the properties of the disk. The next aspect I want to highlight is the discretization method. To comply with the conservation laws, all equations are integrated over a time-dependent Volume V with surface ∂V [15]. These volumes are then subdivided into volume sections between two gridpoints; the so-called finite-volume discretization. Since the star's radiation plays an substantial role in disks behaviour and dynamics (see e.g. [22]), the interaction of radiation and matter is integrated in the equations of the code. The modifications, especially valid for this code, are combined in Sec. 2.2. To treat the viscous effects as matter moving inside the disk, a combination of an artificial viscosity (originally designed to treat shock events properly [13]) and a modification of the physical α model [41] is used (Sec. 2.3 and 2.4). Finally, a grid equation (based on [16]) is solved together with the physical equations to guarantee sufficient gridpoint concentration at regions of physical interest. The derivation of the adaptive grid is shown in Sec. 3.1.

1.3 Protostellar Parameters

For the protostellar radius and luminosity values the work of [36] and [17] is used. The resulting values for the protostellar radius and luminosity over a mass range between 0.1 and 1.0$M_\odot$ can be found in Tab. 1. These values are calculated using stellar evolution models, therefore have limitations and should serve merely as a reference. It is also possible to remodel a specific protostar by taking its mass, radius and luminosity from the respective work.

1.4 Scales in Length and Time

To get a better overview about the physical system of a protoplanetary disk, a schematic representation of the associated length and temporal scales is useful. First, the dimensions of a protoplanetary disk are approximated and thereafter its different temporal scales examined. For the extent of a disk, three parameters are important, since axial symmetry is assumed: the inner and outer radius $r_{\rm in}$ and $r_{\rm out}$ as well as the vertical scale height $H_{\rm p}$.

Inner boundary

The importance of the inner boundary has already been highlighted in [38]. As described in [23], the inner radius is coupled to the stellar magnetic field, which forces the disk material into corotation at the truncation radius $r_{\rm t}$. This material falls quasi freely onto the star via magnetic funnels [23] inside the co-rotation radius $r_{\rm co}$ (see e.g. [19] and Fig. 1);

$$r_{\rm co} = \left(\frac{{\rm G} M_* P^2}{4\pi^2} \right)^{1/3} , \tag{1.4}$$

with the stellar mass M_*, the gravitational constant G and the stellar rotation period P. According to [25], the rotational period for low mass stars is peaking at $\sim$ 2days. This period results in a co-rotation radius of $\sim 4.6{\rm R}_*$ for a star with $1 M_\odot$. For the truncation radius, a relation between r_t and stellar as well as disk parameters can be found (see e.g. [23]):

$$\frac{r_t}{R_*} \sim \frac{B_3^{4/7} R_*^{12/7}}{M_*^{1/7} M_{-8}^{2/7}} \, . \tag{1.5}$$

With B_3 the stellar magnetic field in kG and M_{-8} the accretion rate in $10^{-8} M_\odot$/yr. For typical T-Tauri stars a range of $4 \leq r_{\rm t} \leq 6{\rm R}_*$ can be assumed. Finally, the inner radius of the disk is set to

$$r_{in} = 4 R_* . \tag{1.6}$$

The lower boundary was used for further consideration since it is smaller than the co-rotation radius. In this case the ram pressure is large enough to push the disk beyond the corotation radius. At the point where the magnetic pressure equals the ram pressure, the material is forced in corotation and is accreted onto the star in a

quasi free-fall. The process of breaking up the disk in this way is not yet completely understood and not believed to be axialsymmetric. Nevertheless the density drops so rapidly during the free-fall that these effects are not taken further into account. For $r_\mathrm{t} \geq r_\mathrm{co}$ the material would be blown away in disk winds (see e.g. [23]). The final values for r_in can be found in Tab. 1.

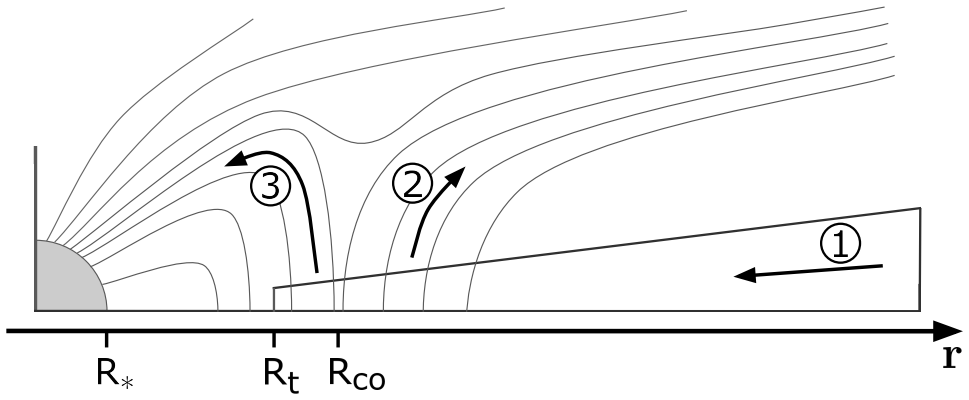

Figure 1: Schematic overview of magnetic accretion onto a young star (grey circle on the left) along the radial axis r; after [12]. The truncation radius R_t symbolizes the inner boundary of the disk and is located at $\sim$ few R_* (R_* being the stellar radius). The disks material is transported towards the inner region of the disk (arrow 1) and further onto the star along magnetic field lines (thin solid lines) for radii between R_t and the corotation radius R_co (arrow 3) or is blown away by ionized winds (for $r > R_\mathrm{co}$, arrow 2).

Outer boundary

The outer radius of the disk r_out is calculated according to the minimum mass solar nebular model (MMSN) [24]. To comply with the MMSN, the goal is to reach 1% of the stellar mass in the disk. According to the MMSN model the surface density scales with $\Sigma \propto r^{-3/2}$ and the mass of the disk M_d can be calculated via

$$M_d = \int_{r_{in}}^{r_{out}} 2\pi r \Sigma_0 \left(\frac{r}{r_0}\right)^{-3/2} \mathrm{dr}. \tag{1.7}$$

A relation for Σ_0 can be found using [4] under the assumption of a steady state disk. From $\Sigma \sim \nu^{-1}$, $\nu = \alpha c_\mathrm{s}^2/\Omega_K$ and $c_\mathrm{s}^2 \sim T \sim r^{-3/4}L^{1/4}$ for a thin disk one gets:

$$\Sigma_0 \sim \left(\frac{M_*}{M_\odot}\right)^{1/2} \left(\frac{L_*}{L_\odot}\right)^{-1/4} \tag{1.8}$$

The constant of proportionality can be eliminated with the initial value given in the MMSN model for our sun at 1AU of $\Sigma_{0,\odot} = 1700\text{g/cm}^2$ [24]. The relation in Eq. 1.8 changes to

$$\Sigma_0 = 1700\left(\frac{M_*}{M_\odot}\right)^{1/2}\left(\frac{L_*}{L_\odot}\right)^{-1/4}\left(\frac{r}{\text{AU}}\right)^{-3/2}. \tag{1.9}$$

The resulting values for r_{out} and the surface density at this outer radius can be found in Tab. 1. To check, if these values are plausible, they can be compared to ALMA data regarding T-Tauri stars. In [3] disk radii from 10 to 100AU are found which is in consensus with the calculated values in this chapter. These values however, have to be seen as a reference and they are not reflecting realistic disks in all cases. For example, the surface densities for higher disk masses are quiet low and the disk would have already lost its identity in the ISM. Furthermore, the inner radius is calculated in Tab. 1 with approximate values. During a simulation the massflow changes and thus the inner radius does. An more realistic treatment of the boundaries is given in Section 3.4.

Table 1: Reference values for a range of stellar masses and disk properties, the disk mass is fixed by $0.01M_*$.

M_* [$M_\odot$]	R_* [$R_\odot$]	L_* [$L_\odot$]	r_{in} [AU]	r_{out} [AU]	Σ_{out} [g/cm^2]
0.1	2.49	0.604	0.046	1.41	362.9
0.2	2.52	1.042	0.047	3.64	108.5
0.4	2.70	1.633	0.050	9.04	34.5
0.6	3.53	2.748	0.066	17.6	13.9
0.8	4.30	4.909	0.080	31.3	5.85
1.0	4.88	6.887	0.091	46.2	3.34

Vertical structure

The vertical structure is determined by the pressure scale height H_{P}. It is calculated through the hydrostatic equilibrium in which the pressure force counteracts gravity exerted by the central star (see e.g. [4]):

$$\frac{dP}{dz} = -\rho\frac{GM_*z}{(r^2+z^2)^{3/2}}\,. \tag{1.10}$$

Now two of the key assumptions mentioned earlier can be used. First, $((r^2+z^2)^{3/2}) = r^3$ due to the thin disk approximation. And second the internal energy is constant in z, so the pressure can be written as $P = \rho RT = \rho e(\gamma - 1)$ for an ideal gas, where only P and ρ depend on z. Eq. 1.10 can now be rewritten to:

$$\frac{1}{\rho}\frac{d\rho}{dz} = -\frac{z}{H_{\mathrm{P}}^2}\,, \tag{1.11}$$

with

$$H_{\mathrm{P}}(r) = \sqrt{\frac{e(\gamma-1)r^3}{\mathrm{G}M_*}} = \sqrt{\frac{TRr^3}{\mathrm{G}\,M_*}} \tag{1.12}$$

The temperature has already been estimated in the previous subsection and with $R = \mathcal{R}/\mu$ ($\mathcal{R}$ as universal gas constant and μ as the mean molecular weight) the scale height can be approximated with

$$H_{\mathrm{P}}(r) \sim 0.8 \cdot 10^{12}\mathrm{cm}\left(\frac{r}{\mathrm{AU}}\right)^{\frac{5}{4}}\left(\frac{L_*}{\mathrm{L}_\odot}\right)^{\frac{1}{8}}\left(\frac{M_*}{\mathrm{M}_\odot}\right)^{-\frac{1}{2}}\,, \tag{1.13}$$

which results in a H_{P}/r ratio of ~ 0.05 at $r = 1$ AU for a solar like star.

Timescales

Despite from global timescales (e.g. the total lifetime of a protoplanetary disk), there are several other timescales which are important for protoplanetary disks:

- *Orbital timescale:* The period of which a test mass can orbit around the star is defined by the Kepler timescale

$$\tau_{\mathrm{K}} = 2\pi\Omega_{\mathrm{K}}^{-1} = 2\pi\sqrt{\frac{r^3}{\mathrm{G}M_*}} \sim 1 \text{ year at 1 AU and 1 } \mathrm{M}_\odot\,, \tag{1.14}$$

  where Ω_{K} represents the Keplerian angular velocity of the test mass at a certain radius.

- *Viscous timescale:* In a viscous disk an accretion related process depends on the viscous timescale $\tau_\nu = r^2/\nu$ (see e.g. [4]) which can be approximated with the α-model [41] (α usually set to 0.01 e.g. [30]). The viscous timescale is a

measure for the time in which matter diffuses in a disk at a radius r. According to [27],

$$\tau_\nu \propto r^{5/4}\,, \tag{1.15}$$

the viscous timescale extends nearly over 3 orders of magnitude for the radial range of the disk (radius values from Tab. 1 for a $1\mathrm{M}_*$ star).

- *CFL timescale:* According to the CFL condition [14] the respective timestep limitation writes [15]

$$\tau_{\mathrm{CFL}} = \min_{\text{all cells}} \frac{\Delta x}{|u| + c_\mathrm{s}}\,. \tag{1.16}$$

The absolute value of the velocity can be approximated with $|u|+c_\mathrm{s} = u_\varphi = r\Omega_\mathrm{K}$, since $u_\varphi \gg u_\mathrm{r}, c_\mathrm{s}$. For a solar like star and a grid spacing in φ-direction of ~ 0.04 AU (this is the equivalent of 200 gridpoints), the timestep for quantities at 1 AU is limited by $\tau_{\mathrm{CFL}} \sim 10^5$ s $\ll \tau_\nu$. This timestep decreases further when moving closer to the star. At 0.1 AU $\tau_{\mathrm{CFL}} \sim 3 \cdot 10^4$ s and thus utilizing an explicit scheme results in long computation times.

- *Total lifetime:* Finally, the total lifetime of a disk's gas component can be estimated based on observations of the fraction of stars with near-infrared access as a function of the age of the stellar group (see e.g. [26]): $\tau_{\mathrm{tot}} < 10^7$ years

2 Equations and Discretization

In this chapter the physical equations as well as their discretization are outlined. Furthermore, the viscosity model and the effect of stellar irradiation is described.

2.1 Physical Equations of RHD, Opacity and EOS

To describe the dynamic interaction of radiation and matter in the disk the equations of radiative hydrodynamics (RHD) are adapted for cylindrical geometry (see [15]). All velocities are assumed non relativistic, the coordinate system is Eulerian and for the radiation terms a local thermal equilibrium (LTE) source function is used. The RHD equations, used to calculate four primary variables: surface density Σ, radial velocity u_{r}, angular velocity u_φ and internal energy e, can be written as e.g. [29] or [38]:

Equation of Continuity

$$\frac{\partial \Sigma}{\partial t} + \frac{1}{r}\frac{\partial}{\partial r}\left(r u_r \Sigma\right) = 0\,. \tag{2.1}$$

Equation of Motion

The radial component of the equation of motion (2.2) with the gas pressure P (vertically integrated and obtained from tables), the gradient of the total gravitational potential $\partial_r \Phi_{\mathrm{tot}} = \partial_r \Phi_* + \partial \Phi_{\mathrm{disk}}$ combining the potentials of the star and the disk as well as the radial and angular parts of the viscous pressure tensor Q_{rr} and $Q_{\varphi\varphi}$. The radiative pressure term is omitted since its contribution is much smaller than the gas pressure (see e.g. [31]).

$$\frac{\partial}{\partial t}\left(\Sigma u_r\right) + \frac{1}{r}\frac{\partial}{\partial r}\left(r\,\Sigma\,u_r^2\right) - \frac{\Sigma\,u_\varphi^2}{r} + \frac{\partial P}{\partial r} + \Sigma\frac{\partial}{\partial r}\Phi_{\mathrm{tot}} + \frac{1}{r}\frac{\partial}{\partial r}\left(r\,Q_{rr}\right) - \frac{Q_{\varphi\varphi}}{r} = 0\,, \tag{2.2}$$

The angular component with the respective parts of the viscous pressure tensor $Q_{r\varphi}$ as well as $Q_{\varphi r}$.

$$\frac{\partial}{\partial t}(r\Sigma u_\varphi) + \frac{1}{r}\frac{\partial}{\partial r}\left(r^2 \Sigma u_r u_\varphi\right) + \frac{\partial}{\partial r}\left(r\,Q_{r\varphi}\right) + Q_{\varphi r} = 0\,. \tag{2.3}$$

Equation of internal Energy

$$\frac{\partial}{\partial t}\left(\Sigma e_r\right) + \frac{1}{r}\frac{\partial}{\partial r}\left(r u_r \Sigma e_r\right) + P\frac{1}{r}\frac{\partial}{\partial r}\left(r u_r \Sigma\right) + \epsilon_Q \\ - 4\pi\kappa_{\mathrm{P}}\left(J_0 - S\right) + \Delta E_{\mathrm{rad}} = 0\,, \quad (2.4)$$

with the gas pressure P, the energy generated by viscous stress $\epsilon_Q = \mathbf{Q} : \nabla\mathbf{u}$, the Planck opacity κ_{P}, a source function S and the radiative heating/cooling term ΔE_{rad} which is reviewed in Sec. 2.6.

Equation of Radiative Energy

$$\frac{\partial}{\partial t}J_0 \;+\; \frac{1}{r}\frac{\partial}{\partial r}(r u_r J_0) \;+\; c\frac{1}{r}\frac{\partial}{\partial r}(r H_{r,0}) \;+\; \epsilon_{\mathrm{K}} \;+\; c\kappa_{\mathrm{P}}\rho_0(J_0 \;-\; S) \quad = \quad 0\;, \quad (2.5)$$

with $\epsilon_K = \mathbf{K} : \nabla\mathbf{u}$ the radiative energy generated by the radiative pressure $\mathbf{K}$. As well as the radiation temperature J_0 and the radiation flux $H_{r,0}$ both evaluated at the midplane of the disk (here the Eddington variables are used, see e.g. [34]).

Equation of Radiative Flux

$$\frac{\partial}{\partial t}H_{r,0} \;+\; \frac{1}{r}\frac{\partial}{\partial r}(r u_r H_{r,0}) \;+\; c\frac{1}{r}\frac{\partial}{\partial r}(r K_{r,0}) \;+\; \epsilon_{\mathrm{H}} \;+\; c\kappa_{\mathrm{R}}\rho_0 H_{r,0} \quad = \quad 0\;, \quad (2.6)$$

with the radial part of the radiative pressure $K_{r,0}$ (again as Eddington variable, see e.g. [34]), the Rosseland mean opacity κ_{R} [33] and $\epsilon_{\mathrm{H}} = H_{r,0}\frac{\partial u_r}{\partial r}$. The source function $S = \sigma/\pi T^4$ follows the Stefan-Boltzmann-Law and the viscous pressure tensor Q_{ij} is further explained in Sec. 2.3. Finally, this set of equations needs closing conditions: opacities, equations of state (EOS) and, to close the radiative equation, the Eddington factor f_{edd}. To avoid solving the radiation transport equation f_{edd} is fixed to $1/3$, which is the Eddington approximation (see e.g. [15]). The equation of state, which connects density and temperature, as well as the opacities, is given in tables. These tables are entered with the midplane density values.

2.2 Simplified Interaction of Radiation and Matter

According to [38], it is possible to approximate the radiative transport in Eq. 2.5 by its dominant terms. Thus the radiative equations must not be treated individually and can be directly implemented into the Eq. 2.4. The disk's heating and therefore

the internal energy balance as well as the temperature structure is dominated by the radiation of the central star (e.g. [22]). Assuming a stationary limit for the radiative equations, the temporal, the advection and the velocity terms can be neglected. Hence, only the dominant terms in Eq. 2.5 remain.

$$c\frac{1}{r}\frac{\partial}{\partial r}(rH_{r,0}) + c\kappa_P\rho_0(J_0 - S) = 0 \tag{2.7}$$

After multiplying 4π to both sides, the radiative term in the energy equation reads.

$$4\pi\kappa_P\rho_0(J_0 - S) = -4\pi\frac{1}{r}\frac{\partial}{\partial r}(rH_{r,0})\,. \tag{2.8}$$

Now, $H_{r,0}$ has to be expressed by reducing the radiative flux equation in the same way. After dropping the temporal, the advection and the velocity terms, we receive:

$$c\,\partial_r K_{rr} + c\kappa_R\rho_0 H_{r,0} = 0\,. \tag{2.9}$$

Dropping c and using the Eddington approximation ($f_{edd} = 1/3 = K_{rr}/J_0$), we get

$$\partial_r(f_{edd}J_0) + \kappa_R\rho_0 H_{r,0} = 0\,. \tag{2.10}$$

The equation of radiation flux is modified s0 that J_0 is replaced with $S = \sigma/\pi T_0^4$ and Eq. 2.9 and Eq. 2.10 can be combined to find an expression for $H_{r,0}$,

$$H_{r,0} = -\frac{f_{edd}\sigma\partial_r(T_0^4)}{\pi\kappa_R\rho_0}\,. \tag{2.11}$$

Finally, the radiative term in the equation of energy Eq. 2.4 can be replaced by inserting Eq. 2.11 into Eq. 2.8

$$4\pi\kappa_P(J_0 - S) = -4\pi\frac{1}{r}\partial_r\left(-r\frac{f_{edd}\sigma\partial_r(T^4)}{\pi\kappa_R\rho_0}\right). \tag{2.12}$$

2.3 Artificial Viscosity Model

The basic model for the artificial viscosity used in the TAPIR code is based on the work of e.g. [13]. In this formulation the origin of the viscosity term is derived from complete inelastic collisions of two point masses. The resulting viscosity model follows some important conditions. Viscosity only acts dissipating, converts kinetic energy into heat when there is contraction and becomes zero during expansion. Additionally,

viscosity disappears during self-similar-motion such as uniform compression and rigid rotation. Considering the complete inelastic collision of two masses M_1 and M_2, the kinetic energy decreases by the portion of $\mu(\Delta u)^2/2$, with the reduced mass μ and the initial difference of the velocities of the two masses Δu. According to [13], the basic form of the the artificial viscosity can be written as

$$Q = c_1 \rho c_\mathrm{s} |\Delta u| + c_2 \rho (\Delta u)^2 \,, \tag{2.13}$$

where c_1 and c_2 are constants, c_s is the speed of sound and ρ the gas density. The non linear term has the same form as the loss of kinetic energy during an inelastic collision, with density acting as the reduced mass. It shall help to satisfy the shock conditions, whereas the linear term prevents nonphysical oscillations as a damping part. To use this formulation in the TAPIR code, some adaptions must be made. First, the nonlinear term can be neglected since there are no strong shocks expected in a protoplanetary disk. The artificial viscosity reduces to the linear term only

$$Q = c_1 \rho c_s |\Delta u|. \tag{2.14}$$

One problem of this formulation is that the artificial viscosity does not vanish for uniform compression, since the linear term is always present as a damping part of the viscosity. Keeping the artificial viscosity close to the physical viscosity can solve this problem. With $\Delta u = l_z q$, where l_z is a typical length scale and q is the strain-rate-tensor, Eq. 2.14 becomes

$$\begin{aligned} Q_{ij} &= c_1 \rho c_s l_z q_\mathrm{ij} \,, \\ q_{ij} &= \frac{1}{2}\left(\frac{\partial u_i}{\partial x_j} + \frac{\partial u_j}{\partial x_i}\right) - \frac{1}{2}\delta_{ij}\mathrm{div}(u) \,. \end{aligned} \tag{2.15}$$

The tensor q_ij now vanishes for rigid rotation and uniform compression since it is constructed according to meet these requirements. To evaluate the remaining constant c_1, the coefficient of the dynamic viscosity has to be calculated. A model of the physical viscosity used in the TAPIR code is presented in the next section.

2.4 Physical Viscosity Model

In a disk turbulent forces transport material inwards. The timescale of these accretion processes are already estimated in Sec. 1.4 and is much longer than an orbital period. The usual description of viscosity ν according to [41] (α-model) is

$$\nu = \alpha c_{\mathrm{s}} H_p \,. \tag{2.16}$$

The basic idea is that turbulent cells are moving with the speed of sound c_{s} up to a maximum extent of the pressure scale height H_p, scaled with the free parameter α. A typical value for this parameter is $\alpha \sim 0.01$ (e.g. [30]). In this TAPIR code the α-model is enhanced with several physical features of the layered disk model [20]. First, the viscosity is divided into a turbulent part which is activated under certain conditions, and a small base value $\alpha_{\mathrm{base}} \sim 10^{-5}$ [21], which is always active. The turbulent activated part itself is also divided into a magneto rotational unstable (MRI, [8]) and a gravitational unstable (GI) part. A GI activates in case the Toomre parameter Q_{T} [42] exceeds a critical value $Q_{\mathrm{crit}} = 1.0$ with

$$Q_T = \frac{c_{\mathrm{s}}\Omega}{\pi \mathrm{G}\Sigma} \,. \tag{2.17}$$

With the assumption of an adiabatic sound speed $c_{\mathrm{s}}^2 = P/\rho = e(\gamma - 1)$ (internal energy e and adiabatic index γ) and the Kepler velocity $\Omega = \sqrt{\mathrm{G}M_*/r^3}$ Eq. 2.17 changes to

$$Q_T = \sqrt{\frac{e(\gamma-1)M_*}{r^3 \mathrm{G}}} \frac{1}{\pi\Sigma} \tag{2.18}$$

and the α-value for GIs α_{GI} yields

$$\alpha_{GI} = \begin{cases} \alpha_{GI,0}(\frac{Q_T}{Q_{crit}} - 1) & \text{for } Q_T > Q_{crit} \\ 0 & \text{else} \end{cases} \,, \tag{2.19}$$

where $\alpha_{\mathrm{GI},0} \ll 1$ [48] and thus is set to $\alpha_{\mathrm{GI},0} = 0.01$.
The MRI distinguishes between turbulence in the surface layer of the disk caused by ionization through stellar irradiation with a maximum surface layer thickness of $\Sigma_{layer} = 100\mathrm{g/cm}^2$ (e.g. [20]), and an instability in the midplane which is activated when the temperature exceeds a critical value $T_{\mathrm{crit}} \sim 1500\mathrm{K}$ (see e.g. [6] or [20]). Since the star is constantly illuminating the disk, the viscosity in the disk's surface layer is always active with $\alpha_{\mathrm{MRI}} = 0.01$. For the activation in the midplane (deep layers) a switch s_{T} has to be added, that allows a smooth transition over $\delta T = 100\mathrm{K}$ from

the non active to the active regions. The following function meets this requirements sufficiently

$$s_T = \frac{1}{2}\left(1 + \tanh \frac{T_{gas} - T_{crit}}{\delta T}\right). \tag{2.20}$$

The combination of the surface layer, the deep layer, the gravitational unstable contribution and the base value gives the total α-parameter:

$$\Sigma\alpha = \Sigma_{\text{layer}}\alpha_{\text{MRI}} + s_T\Sigma_{\text{deep}}\alpha_{\text{MRI}} + \Sigma\alpha_{\text{GI}} + \Sigma\alpha_{\text{base}} \tag{2.21}$$

with $\Sigma_{\text{deep}} = \Sigma - \Sigma_{\text{layer}}$. To combine the artificial and physical viscosity model the factors $c_1 c_s l_z$ in eq. 2.15 are replaced with ν. As $\nu \gg 0$ over the whole radial range and no shocks are expected in a protoplanetary disk, no additional artificial viscosity has to be added.

2.5 Discretization

The discretization is based on a finite volume discretization as presented in [15]. In the TAPIR code, these principles are adapted for cylindrical geometry. An overview of the computational domain is given in Fig. 2. The grid is adapted according to the staggered mesh, with scalar quantities (e.g. Σ) between two gridpoints in a finite, scalar volume and vector quantities (e.g. u_{r}) located at the cell boundaries. To transform the RHD equations into their discrete form, the first step is to integrate them over a time-dependent volume V with surface ∂V and surface element dS. Due to the adaptive grid and the resulting relative velocity between the gas and the gridpoints, the Reynolds transport theorem has to be adapted too [35],

$$\frac{d}{dt}\left(\int_V f\, dV\right) = \int_V \left[\partial_t f + \nabla\cdot\left(f u^{\text{grid}}\right)\right] dV. \tag{2.22}$$

The following notation is used for all discrete quantities: δ denotes a temporal (e.g. δt is the timestep between two simulation models) and Δ a spatial difference as well as $\bar{X}$ are averaged values in the staggered mesh.

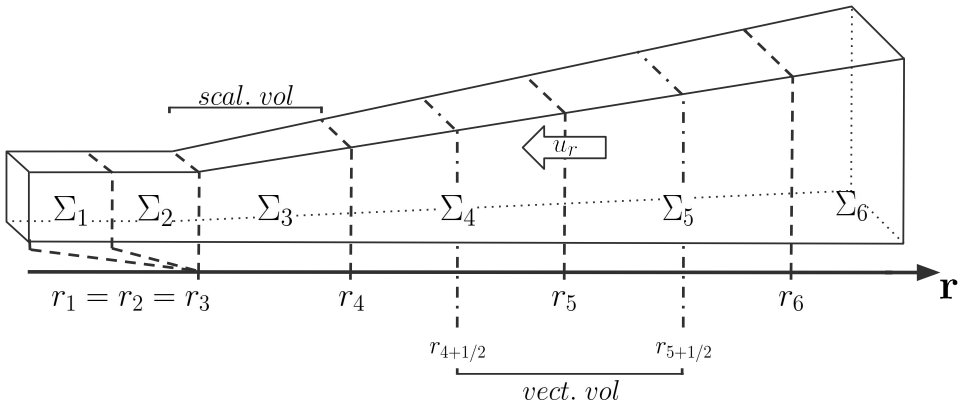

Figure 2: The overall picture of the discretization of the inner part of a cylindrical configuration. The axis r shows the physical domain with the inner boundary at r_3. The cells outside the physical domain (ghostcells with Σ_1 and Σ_2) are defined by boundary conditions and have zero volume. Scalar radii are named with full integer steps r_i, whereas radii defining vectoral volumes are named in half steps $r_{i+1/2}$. As an example for a scalar quantity the surface density is used between two scalar radii. And the velocity in radial direction u_r is defined at a cell boundary within a vectoral volume. The situation is analogue for the outer boundary.

During the simulation, physical quantities are transported across the boundaries of grid cells. Since the adaptive grid moves the grid points, the transport is done with a relative velocity $u_\mathrm{rel} = u - u^\mathrm{grid}$ and not with the gas velocity. According to [15] the advection of a physical quantity X, using finite volumes, is discretized by

$$\int_{\partial V} X u_{rel} dS = \sum \widetilde{X^\mathrm{ad}} \frac{\Delta \mathrm{V}}{\delta t} \,, \tag{2.23}$$

with the advected quantity $\widetilde{X^\mathrm{ad}}$.
The advected volume ΔV ,transported over the cell boundaries, depends on the type of the physical quantity. For a scalar quantity the grid cell volume (see Fig. 2) is defined as $\mathrm{V_s} = \pi(r_{\mathrm{i}+1}^2 - r_\mathrm{i}^2)$ and corresponding advected flux reads $\Delta \mathrm{V_s} = 2\pi u_\mathrm{i} r_\mathrm{i} \delta t - \pi \delta(r_\mathrm{i}^2)$. In case of vectoral quantities, the cell volume, which is defined on the scalar grid, reads $\mathrm{V_v} = \frac{\pi}{2}(r_{\mathrm{i}+1}^2 - r_{\mathrm{i}-1}^2)$ and thus $\Delta \mathrm{V_v} = \frac{2\pi}{2}(r_\mathrm{i} u_\mathrm{i} + r_{\mathrm{i}+1} u_{\mathrm{i}+1}) - \frac{\pi}{2}\delta(r_\mathrm{i}^2 + r_{\mathrm{i}+1}^2)$. The advection scheme utilized in this work is the so-called van Leer scheme [44]. Following these authors, the advected quantity at a grid point i writes

$$\widetilde{X_i^{ad}} = \begin{cases} X_{i-1}^{ad} \text{ , if } u_i^{rel} < 0 \\ X_i^{ad} \text{ , otherwise} \end{cases} \,, \tag{2.24}$$

with

$$X_i^{ad} = X_i + \begin{cases} \frac{\Delta X_i \Delta X_{i-1}}{0.5(X_{i-1} - X_{i+1})} \text{ , if } \Delta X_i \Delta X_{i-1} > 0 \\ 0 \text{ , otherwise} \end{cases} \quad . \tag{2.25}$$

The advected quantities in their different forms (scalar or vectoral) can depend on 5 indices; $i-2$, $i-1$, i, $i+1$ and $i+2$. The quantity X has to be calculated at these gridpoints during the implicit method. Therefore, this so-called 5-point stencil [15] enters the Jacobi matrix. To calculate boundaries of the computational domain, the 5-point stencil requires the implementation of two ghost cells (see Fig. 2). These ghost cells have no volume and are defined by the boundary conditions. The discretization of the RHD equations is shown on the example of the equation of continuity. The remaining set of RHD equations is derived according to [15] or [38]. Introductory, some basic expressions (divergence and gradient) are shown in their discrete form. The divergence of vector quantity $\vec{X}$ can be written in cylindrical coordinates as

$$\int_V \vec{\nabla} \cdot \vec{X} dV = \int_{r_i}^{r_{i+1}} \frac{1}{r} \partial_r (r X_r) 2\pi r dr = 2\pi \Delta (r X_r) \tag{2.26}$$

and the gradient of X changes to

$$\int_V \vec{\nabla} X dV = \int_{r_i}^{r_{i+1}} \partial_r (X) 2\pi r dr = 2\pi r \Delta X \, . \tag{2.27}$$

Equation of Continuity

Applying the Gauß-Theorem to the volume integrated form of the equation of continuity (Eq. 2.1) gives

$$\int_V \partial_t \Sigma dV + \int_{\partial V} \Sigma u_r dS = 0 \, . \tag{2.28}$$

Further applying of the Reynolds Theorem (Eq. 2.22) to Eq. 2.28 leads to

$$\frac{d}{dt} \int_V \Sigma dV + \int_{\partial V} \Sigma \left(u_r - u^{\mathrm{grid}} \right) \, , \tag{2.29}$$

with the radial gas velocity u_{r} and the velocity of the grid points u^{grid}. Finally, applying Eq. 2.23 and multiplying with the time-step the discrete form of the equation of continuity summed up over all grid points is

$$\delta[\Sigma \, V_{\mathrm{s}}] + \sum \widetilde{\Sigma} \, \Delta \mathrm{V}_{\mathrm{s}} = 0 \, , \tag{2.30}$$

with the temporal change in the surface density multiplied with the scalar volume $\delta[\Sigma\, V_\mathrm{s}]$ and the sum over all advected surface densities $\widetilde{\Sigma}$.

Equation of Motion

The radial component of the equation of motion in discrete form is

$$\delta[\overline{\Sigma} u_r\, V_\mathrm{v}] + \sum \widetilde{\overline{\Sigma} u_r}\, \Delta \mathrm{V}_\mathrm{v} - \frac{\overline{\Sigma}\, u_\varphi u_\varphi}{r}\, V_\mathrm{v}\, \delta t + 2\pi r\sqrt{2\pi}\Delta\, [H_\mathrm{p} P_\mathrm{gas}]\, \delta t + \partial_r \Psi(r)_{tot}\, \Sigma\, \mathrm{V}_\mathrm{v}\, \delta t - \frac{\pi}{r}\Delta\left\{ \overline{r}^2\, \mu_\mathrm{Qr} \left[\frac{\Delta u_r}{\Delta r} - \frac{\overline{u}_r}{\overline{r}} \right] \right\} \delta t = 0\,, \quad (2.31)$$

with the following terms from left to right: temporal difference, advection term, centrifugal force, vertical integrated gas pressure force, gravitational acceleration with $\Psi_\mathrm{tot} = \Psi_\mathrm{star} + \Psi_\mathrm{disk}$ ($\Psi_\mathrm{star} = -\mathrm{G}M_*/r$; for Ψ_disk see sec. 4) and the viscosity with the radial scaling factor $\mu_\mathrm{Qr} = \alpha \Sigma c_\mathrm{s} H_\mathrm{p}$ (see eq. 2.16). The φ-component of the equation of motion reads

$$\delta[r\overline{\Sigma} u_\varphi\, V_\mathrm{v}] + \sum r\widetilde{\overline{\Sigma} u_\varphi}\, \Delta \mathrm{V}_\mathrm{v} - \pi\Delta\left\{ \overline{r}^2\, \mu_\mathrm{Q\varphi} \left[\frac{\Delta u_\varphi}{\Delta r} - \frac{\overline{u}_\varphi}{\overline{r}} \right] \right\} \delta t = 0\,, \quad (2.32)$$

with the temporal difference, advection and viscosity using the angular scaling factor $\mu_{\mathrm{Q}\varphi}$.

Equation of internal Energy

Using the assumptions from Sec. 2.2 the discrete internal energy equations reads

$$\delta[\Sigma e\, V_\mathrm{s}] + \sum \widetilde{(\Sigma e)}\, \Delta \mathrm{V}_\mathrm{s} + P\, 2\pi\Delta(r u_\mathrm{r})\, \delta t + 8\pi^2\sqrt{2\pi}\, H_\mathrm{p}\, \sigma\, \Delta \left(-\frac{\frac{2}{3} r^2\, \Delta(T^4)}{\overline{\kappa_\mathrm{R}\rho_0}\, V_\mathrm{v}} \right) \delta t - \frac{\mu_Q}{2} \left\{ \left[\frac{\Delta u_r}{\Delta r} - \frac{\overline{u}_r}{\overline{r}} \right]^2 + \left[\frac{\Delta u_\varphi}{\Delta r} - \frac{\overline{u}_\varphi}{\overline{r}} \right]^2 \right\} V_\mathrm{s}\, \delta t + \Delta E_{rad} \delta t = 0\,, \quad (2.33)$$

with the temporal difference, advection, pressure term, radiative heating/cooling, viscosity with the scaling factor $\mu_Q = \mu_\mathrm{Qr} + \mu_{\mathrm{Q}\varphi}$ and the contribution of stellar heating on the disk's surface ΔE_{rad} which is calculated in Sec. 2.6.

2.6 Irradiation from central star and cooling

Heating, through irradiation from the central star, and cooling at the disk's surface change the thermal profile of the protoplanetary disk. Thus, the structure of the disk is affected (e.g. through the mass flux $\dot{M}(r)$). As protoplanetary disks are optically thick in radial direction (see e.g. [38]), the stellar irradiation has minor influence. In vertical direction however, stellar radiative energy, transported vertically within the disk, is the dominant contributor for calculating ΔE_{rad} in Eq. 2.33. The basic idea of the irradiation can be seen in Fig. 3. Using the equilibrium

$$E_{irr} + E_{amb} - E_{cool} + F_{vert} = 0 \tag{2.34}$$

and following [38], ΔE_{rad} yields

$$\Delta E_{rad} = 2\sigma \frac{1}{1+\tau'}(T_0^4 - T_{amb}^4)\delta t - \frac{1}{1+\tau'} L_* f_{irr} \max\left[\Delta\left(\frac{H_\mathrm{P} - H_*}{r}\right), 0\right]\delta t\,, \tag{2.35}$$

with σ the Stefan-Boltzmann constant, $\tau' = 3/4\tau$ with the optical depth τ according to e.g. [38], midplane temperature T_0, ambient temperature T_amb, timestep δt, stellar luminosity L_*, factor for irradiation efficiency $0 \leq f_\mathrm{irr} \leq 1$, scale height H_P and H_*, which takes a actual size of the central star into account.

2.7 Summary

In this section, the physical model, used in the TAPIR code, is summarized. The RHD equations are shown including a viscosity description according to the α-model, modified for layered accretion. The RHD equations have been discretized by utilizing a finite volume volume discretization. Furthermore, the influence of stellar irradiation on the thermal profile is explained, since it plays a dominant role in heating/cooling the disk. The next section will summarize some numerical aspects utilized in the TAPIR code.

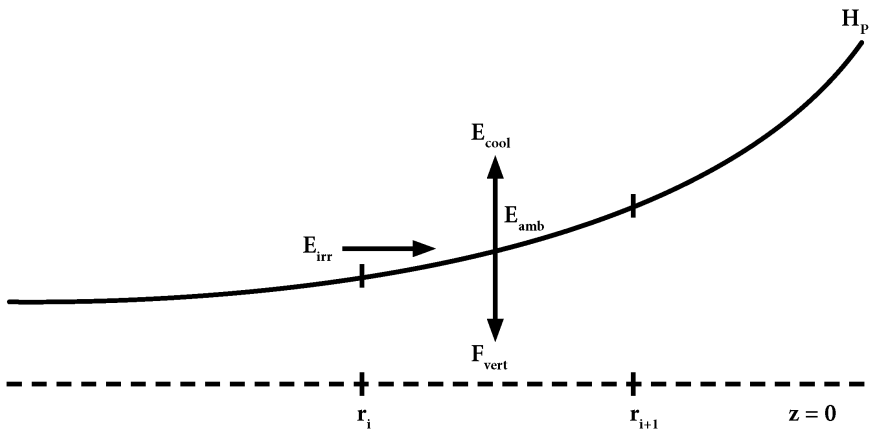

Figure 3: A schematic depiction of the surface heating/cooling caused by stellar irradiation $E_{\rm irr}$ on a surface at scale height $H_{\rm P}$ over the midplane at $z = 0$ between two gridpoints $r_{\rm i}$ and r_{i+1}. The stars light hits the disk under a very shallow angle which depends on the inclination of the disk and the stars radius and therefore on the inclination of the line of sight. Showing the cooling $E_{\rm cool}$ the vertical transported $F_{\rm vert}$ and the ambient radiation $E_{\rm amb}$.

3 Numerical Method

This chapter lists and briefly summarizes some numerical components, utilized in the TAPIR code. For more in depth information on each topic, the respective references are given.

3.1 Adaptive Grid

During a simulation, the structure of the protoplanetary disk is subject to changes (e.g. during an episodic accretion event, see e.g. [6] or [9]). To ensure sufficient gridpoint concentration in radial direction, an adaptive grid is utilized in the TAPIR code. According to [16], the arc-length of a variable X between two gridpoints should be kept constant. This results in a higher grid-point concentration near steeper gradients. This behaviour is illustrated in Fig. 4. Along the radial axis (r) an arbitrary variable $X(r)$ is increased at r_0 to represent a steeper gradient, compared to $X(r) = \text{const.}$ elsewhere. The grey dots indicate an uniform gridpoint distribution with the same radial distance between two gridpoints. In the vicinity of r_0 the arc-length between two grey grid-points is much larger, compared to the outer regions. The black dots represent a grid-point distribution with a constant arc-length, resulting in a higher grid resolution close to r_0 (well recognizable by the vertical dashed lines, indicating the position of the black dots on the radial axis) while the grid resolution decreases towards the radial edges. The redistribution of gridpoints, however, can not occur instantaneously. According to [16], abruptly changing the grid-point position can result in numeric instabilities. Therefore, the adaptive grid is spatial and temporal smoothed (for details see [16]).
In Fig. 5 the redistribution of grid-points during an actual simulation is illustrated. The setup is similar to Fig.4. A uniform surface density Σ distribution is increased at r_0 (see upper part of Fig. 5). To achieve sufficient resolution in the vicinity of r_0, the grid-points (indicated by the solid black lines in the lower part of Fig. 5) start to move towards r_0. Here, the temporal smoothing can be observed. For small times ($\log(\mathrm{T}/\mathrm{T}_{\max}) < -6$) the grid-points remain static in a logarithmic equidistant distribution. For times larger than $\log(\mathrm{T}/\mathrm{T}_{\max}) \sim -6$ the redistribution of the grid-points starts. At $\log(\mathrm{T}/\mathrm{T}_{\max}) \sim -3$ the redistribution is completed. The resulting accumulation of grid-points provides sufficient resolution close to r_0.

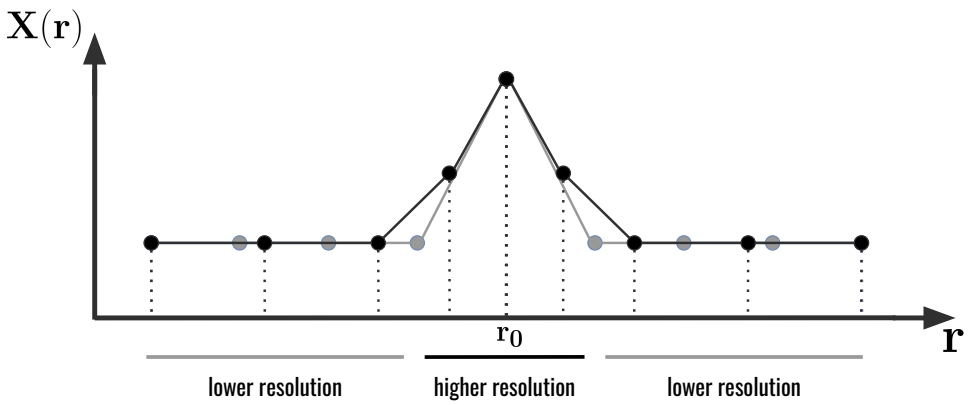

Figure 4: Illustration of the adaptive grid principle. An arbitrary variable $X(r)$ is increased along the radial axis r at a specific point r_0. The grey dots represent a uniform grid-point distribution (same radial distance between two gridpoints). The black dots represent a grid-point distribution with a constant arc-length between two gridpoints.

3.2 Implicit Computation Procedure

The TAPIR code, utilized for this work, is solving five primary variables in $M = 5$ equations at N gridpoints. This results in $M \times N$ unknown variables. All variables at a given timestep t at gridpoint i can be written as ([16])

$$\mathbf{X}^{(t)} = X_i^{(t)} = (\Sigma_i^{(t)}, u_{r,i}^{(t)}, u_{\varphi,i}^{(t)}, e_i^{(t)}, r_i^{(t)}) \,. \tag{3.1}$$

Together with the discrete equations of Sec. 2.5 and 3.1 a nonlinear system of M equations has to be solved

$$\mathcal{G}_m(X_i) = 0 \text{ for } 1 \leq m \leq M \,. \tag{3.2}$$

Following [15], the Newton-Raphson iteration is used to solve this set of equations. $\mathbf{X}^{(t+1)}$ of the new timestep $t+1$ is assumed to solve the equations $\mathcal{G}_m(\mathbf{X}^{(t+1)}) = 0$. This system is then expanded up to the first order around the new solution

$$\mathcal{G}(\mathbf{X}^{(t+1)}) = \mathcal{G}(\mathbf{X}^{(t)}) + \frac{\partial \mathcal{G}}{\partial \mathbf{X}^{(t)}} \left(\mathbf{X}^{(t+1)} - \mathbf{X}^{(t)} \right) = 0 \,. \tag{3.3}$$

Finally, the temporal difference $\delta\mathbf{X} = \mathbf{X}^{(t+1)} - \mathbf{X}^{(t)}$ can be calculated by inverting

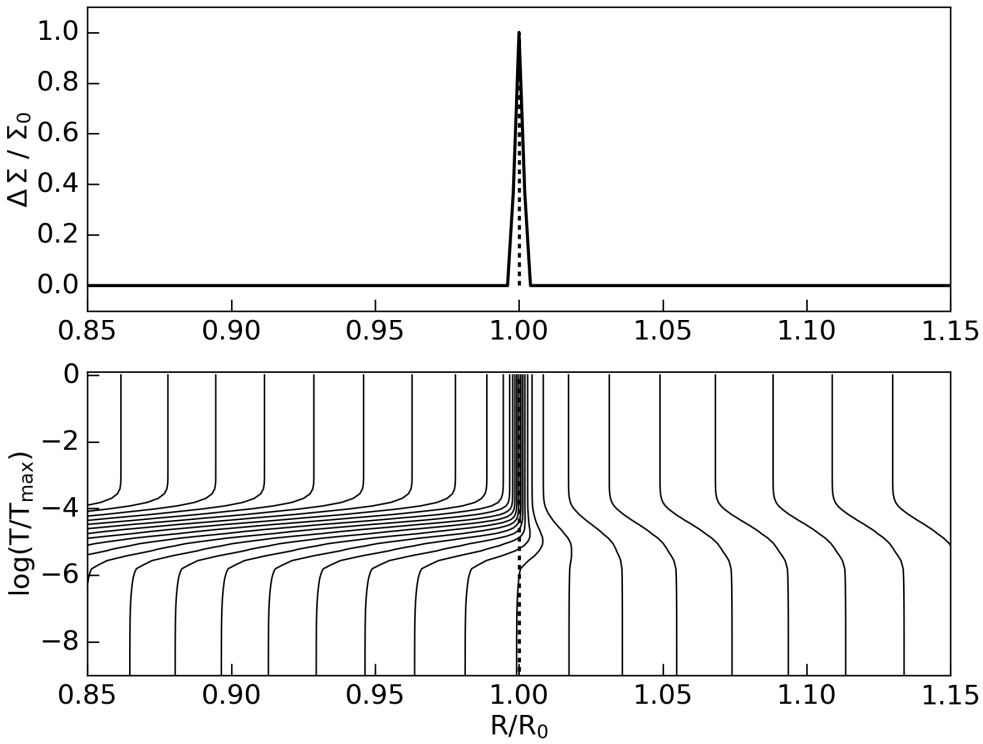

Figure 5: Upper panel: An increase in the surface density at an arbitrary radius R_0 (dashed line). The radius is normed to R_0 and the surface density is normed to the maximum value at the peak. Lower panel: The radius is shown as in the upper part. Each line represents the location of a specific grid point for a time during a simulation T. The time is normed to the maximum time T_{max} (see [38])

.

the Jacobi-matrix $\partial\mathcal{G}/\partial\mathbf{X}$ via:

$$\delta\mathbf{X} = -\left(\frac{\partial\mathcal{G}}{\partial\mathbf{X}^{(t)}}\right)^{-1}\mathcal{G}(\mathbf{X}^{(t)}) \tag{3.4}$$

This procedure is repeated until the relative temporal difference falls below a certain accuracy (usually $\varepsilon < 10^{-6}$). Since a 5-point stencil is used, the adjacent variables at gridpoint $i-2$, $i-1$, $i+1$ and $i+2$ enter the matrix as well to calculate a variable at gridpoint i. All other entries become zero and therefore the matrix has a block penta-diagonal structure

$$\begin{pmatrix} \ddots & \ddots & \ddots & \ddots & \ddots & \ddots & \\ \dots 0 & \frac{\partial\mathcal{G}_{m,i}}{\partial x_{m,i-2}} & \frac{\partial\mathcal{G}_{m,i}}{\partial x_{m,i-1}} & \frac{\partial\mathcal{G}_{m,i}}{\partial x_{m,i}} & \frac{\partial\mathcal{G}_{m,i}}{\partial x_{m,i+1}} & \frac{\partial\mathcal{G}_{m,i}}{\partial x_{m,i+2}} & 0\dots \\ & \ddots & \ddots & \ddots & \ddots & \ddots & \ddots \end{pmatrix}. \tag{3.5}$$

Each of the entries is a $M \times M$ matrix itself. Since the TAPIR code solves five equations, one ends up with a 5×5 submatrix like

$$\frac{\partial\mathcal{G}_{m,i}}{\partial x_{m,i-2}} = \begin{pmatrix} \frac{\partial\mathcal{G}_{1,i}}{\partial x_{1,i-2}} & \frac{\partial\mathcal{G}_{1,i}}{\partial x_{2,i-2}} & \frac{\partial\mathcal{G}_{1,i}}{\partial x_{3,i-2}} & \cdots \\ \frac{\partial\mathcal{G}_{2,i}}{\partial x_{1,i-2}} & \frac{\partial\mathcal{G}_{2,i}}{\partial x_{2,i-2}} & \frac{\partial\mathcal{G}_{2,i}}{\partial x_{3,i-2}} & \cdots \\ \vdots & \vdots & \vdots & \ddots \end{pmatrix}. \tag{3.6}$$

The inversion is done via a conversion of the matrix into an upper triangular block system. For a detailed description of the calculation see [15].

3.3 Initial Model

An implicit numerical method requires a full solution of the system (RHD equations together with an adequate grid-point distribution) to start the computation (see e.g. [15]). For the TAPIR code, we aim to construct a stationary initial model. Since stationary models can be calculated analytically (see e.g. [4]), they can be used to verify the numeric method utilized in the TAPIR code (see [38]). Starting from a Keplerian disk, which has no radial velocity u_r and is in thermal equilibrium in vertical and radial direction, a time-independent mass accretion rate $\dot{M}$ at the outer boundary is chosen. The combination of the stellar parameters (e.g. radius R_*, mass M_* and luminosity L_*) and the boundary conditions (see Sec. 3.4) fully describe the internal structure of the disk. As the viscous timescale τ_ν characterizes the evolution of the surface density (e.g. [5]), τ_ν is the natural timescale for the transition towards the

stationary model. The model is considered to be stationary, as the timestep exceeds $\sim 10\,\tau_\nu$.

3.4 Boundary Conditions

The boundary conditions have to be chosen carefully, since the disk physics change with different boundary conditions [38]. Additionally, the boundary conditions enter the Jacobi-matrix (Eq. 3.5) and have to be chosen to keep the matrix's structure as regular as possible [15]. Especially the inner boundary is crucial (see [38]) since the disk's structure and evolution depends strongly on the flux and temperature at this point. A crucial parameter to define the overall structure of a protoplanetary disk is the massflow (see [38]). The importance of this value can easily be demonstrated using a approximation for a stationary disk, shown in [4], where the massflow is considered to be constant.

$$\dot{M} = const. \propto \nu\Sigma \tag{3.7}$$

Since the viscosity model is already defined (see Sec. 2.4) the massflow directly dictates the surface density profile of the disk and thus its internal structure. The outer disk radius is considered to be located at the point where the disk looses its identity in the ISM. In other words, if the surface density drops to a given value (in the following simulations $\Sigma_{\text{out}} = 20\text{g/cm}^2$ is used), the disk is considered to end. To satisfy these requirements different boundary conditions are set at the inner and outer boundary:

- *Outer boundary:* The surface density as well as the temperature are set to be *open*. Meaning the gradient over the outer boundary for these variables is zero (Van Neumann boundary conditions). This is implemented for an quantity X at the gridpoint i as follows:

  $$X_i - X_{i-1} = 0\ . \tag{3.8}$$

  The velocity in angular direction is set to the Keplerian velocity and the radial velocity is set to keep the massflow constant for the computation of the initial model:

  $$\dot{M} = 2\pi R_i \Sigma_i u_{r,i} = const.\ , \tag{3.9}$$

during the simulation the massflow is set to zero. The last boundary condition to be set at the outer radius is the radius itself. It is simple placed to the point, where the surface density drops below $20\mathrm{g/cm}^2$.

- *Inner boundary:* At the inner edge of the disk the surface density, temperature and the velocity in radial direction are considered to be *open*. The inner radius itself is fixed to the truncation radius (see Eq. 1.5) during the calculation of the initial model and moves according to the changing massflow $\dot{\mathrm{M}}$ during the simulation. The angular velocity at the inner boundary is set to be in corotation with the star.

3.5 Summary

In this section some key numeric features of the TAPIR code are presented. The adaptive grid providing sufficient grid-point resolution for each timestep. An implicit calculation method requiring the inversion of the Jacobi-matrix and an initial model, which already solves the full set of RHD equations. To ensure a successful simulation, the boundary conditions have to be chosen carefully. In the following sections the calculation of the gravitational potential of the disk as well as its implementation into the equations is discussed.

4 Self Gravity of the Disk

To work out the effects of the disk's gravitational potential on the structure and long term evolution of protoplanetary disks, the potential as well as its gradient have to be derived and implemented into the TAPIR code. In this chapter, the gravitational potential and its gradient with respect to the radius of a thin protostellar disk is calculated using complete elliptic integrals. Furthermore, the elliptic integrals and the gravitational potential (including the gradient) in radial direction, are presented in discrete form and the implementation into the model is discussed. Finally, the impact of the potential in vertical direction on the scale height is presented. The angular direction is not effected by the disk's self gravity due to the axial-symmetry.

4.1 Derivation of the Potential

To calculate the potential of a thin disk, the general solution of the Poisson equation

$$\triangle\Phi(\vec{x}) = 4\pi G\rho(\vec{x}) \tag{4.1}$$

is used, using Green's method (analog to [11])

$$\Phi(\vec{x}) = -\mathrm{G}\int \frac{\rho(\vec{x}')}{|\vec{x}-\vec{x}'|} d^3\vec{x}' \,. \tag{4.2}$$

For an axis symmetric disk using cylindrical coordinates with $d^3\vec{x}' = R'dR'd\phi'dz'$ and the surface density $\Sigma = \int \rho dz$ Eq. 4.2 changes to:

$$\Phi(R,\phi,z) = -\mathrm{G}\int_0^\infty \int_0^{2\pi} \frac{\Sigma(R')R'}{|\vec{x}-\vec{x}'|} dR'd\phi' \,, \tag{4.3}$$

with $\vec{x} = (R,\phi,z)$ and $\vec{x}' = (R',\phi',0)$. Now the term $|\vec{x}-\vec{x}'|$ has to be evaluated. The detailed calculation can be found in the appendix (A.1). Introducing $k^2 = 4RR'/((R+R')^2+z^2)$ gives

$$|\vec{x}-\vec{x}'|^2 = [(R+R')^2+z^2][1-k^2\cos^2(\frac{1}{2}\phi')] \,. \tag{4.4}$$

The radial and angular components are now separated and the angular part of the integral in Eq. 4.3 can be transformed. Substituting $t = \cos(\frac{1}{2}\phi')$ and $d\phi' = \frac{-2dt}{\sin(\frac{1}{2}\phi')}$

results in

$$\int_0^{2\pi} \frac{1}{\sqrt{1-k^2\cos^2(\frac{1}{2}\phi')}} d\phi' = 2\int_{-1}^{1} \frac{1}{\sqrt{1-t^2}\sqrt{1-k^2t^2}} dt \,. \tag{4.5}$$

A detailed calculation is is executed in Appendix A.2. Prior the last adaption of this integral, the factor k^2 has to be studied for the different possible values of R, R' and z to show that the integrand is symmetric and real in t. For this it is sufficient to proof the following lemma:

Lemma 1. $k^2 = 4RR'/((R+R')^2+z^2) \leq 1 \;\forall (R, R', z)$.

Proof. w.l.o.g. $z = 0$. Furthermore,

$$\begin{aligned} ((R+R')^2+z^2)/4RR' &\geq 1 \\ R^2+2RR'+R^2 &\geq 4RR' \\ R^2-2RR'+R^2 &\geq 0 \\ (R-R')^2 &\geq 0 \end{aligned} \tag{4.6}$$

is true for all real values of R and R' □

The integrand is shown to be symmetric and real and thus the integral in Eq. 4.5 can be simplified to

$$2\int_{-1}^{1} \frac{1}{\sqrt{1-t^2}\sqrt{1-k^2t^2}} dt = 4\int_{0}^{1} \frac{1}{\sqrt{1-t^2}\sqrt{1-k^2t^2}} dt = 4K(k) \,. \tag{4.7}$$

The exact definition of the complete elliptical integral of the first kind $K(k)$ can be found in Appendix A.3. Finally, the gravitational potential of a protostellar disk writes

$$\begin{aligned} \Phi(R,z) &= -4\mathrm{G}\int_0^\infty \frac{\Sigma(R')R'K(k)}{\sqrt{(R+R')^2+z^2}} dR' \\ &= -2\mathrm{G}\int_0^\infty \Sigma(R')kK(k)\sqrt{\frac{R'}{R}} dR' \,. \end{aligned} \tag{4.8}$$

4.2 Gravitational force

To add the gravitational potential to the equation of motion, the gradient has to be calculated, which reduces (in one dimensional cylindrical coordinates) to the calculation of the derivative with respect to R

$$\frac{\partial\Phi(R)}{\partial R} = -2\mathrm{G}\int_0^\infty \Sigma(R')\sqrt{R'}\frac{\partial}{\partial R}\left(\frac{kK(k)}{\sqrt{R}}\right)dR' \,. \tag{4.9}$$

Using the product rule

$$\begin{aligned}\frac{\partial}{\partial R}\left(\frac{kK(k)}{\sqrt{R}}\right) &= -\frac{1}{2}\frac{K(k)K}{R^{\frac{3}{2}}} + \frac{1}{\sqrt{R}}\frac{\partial(K(k)k)}{\partial R} \\ &= -\frac{1}{2}\frac{K(k)K}{R^{\frac{3}{2}}} + \frac{1}{\sqrt{R}}\frac{\partial(K(k)k)}{\partial k}\frac{\partial k}{\partial R}\,,\end{aligned} \tag{4.10}$$

the gradient yields

$$\frac{\partial\Phi(R)}{\partial R} = \frac{\mathrm{G}}{R^{\frac{3}{2}}}\int_0^\infty \Sigma(R')\sqrt{R'}\left[kK(k) - 2R\frac{\partial(K(k)k)}{\partial k}\frac{\partial k}{\partial R}\right]dR' \,. \tag{4.11}$$

In Appendix A.3 and A.4 these derivatives are calculated as

$$\frac{\partial(K(k)k)}{\partial k} = \frac{E(k)}{1-k^2} \tag{4.12}$$

and

$$2R\frac{\partial k}{\partial R} = \frac{k^3}{4}\left(-\frac{R}{R'} + \frac{R'}{R} + \frac{z^2}{RR'}\right). \tag{4.13}$$

Equation 4.11 can now be transformed into its final form

$$\frac{\partial\Phi(R)}{\partial R} = \frac{\mathrm{G}}{R^{\frac{3}{2}}}\int_0^\infty \Sigma(R')k\sqrt{R'}\left[K(k) - \frac{k^2}{1-k^2}\frac{E(k)}{4}\left(-\frac{R}{R'} + \frac{R'}{R} + \frac{z^2}{RR'}\right)\right]dR' \,. \tag{4.14}$$

4.3 Discrete Complete Elliptic Integrals

The discretization of the complete elliptic integrals is performed with the arithmetic-geometric-mean (AGM) method [28]. The numerical determination of $K(k)$ and $E(k)$ is reduced to an iterative process down to any required accuracy (see [47]). The initial

values are $a_0 = 1$, $b_0 = \sqrt{1-k^2}$ and $c_0 = k$ and the iterations are computed according to

$$\begin{aligned} a_1 &= \frac{a_0 + b_0}{2} \quad \dots \quad a_{n+1} = \frac{a_n + b_n}{2} \\ b_1 &= \sqrt{a_0 b_0} \quad \dots \quad b_{n+1} = \sqrt{a_n b_n} \\ c_1 &= \frac{a_0 - b_0}{2} \quad \dots \quad c_{n+1} = \frac{a_n - b_n}{2}\,. \end{aligned} \tag{4.15}$$

With every iteration a_n and b_n are approaching the same value M and after the desired number of steps (in the order of 10 [47]) $a_n \sim b_n \sim M$ applies. The complete elliptical integrals can then be numerically evaluated with

$$\begin{aligned} K(k) &= \frac{\pi}{2M}\,, \\ E(k) &= \frac{\pi}{4M}(2 - c_0^2 - 2c_1^2 - \dots - 2^n c_n^2)\,. \end{aligned} \tag{4.16}$$

The $K(k)$ has a singularity at $k = 1$. In [47] this problem was bypassed by setting the exact value for $E(1) = 1$ as well as a large value for $K(k = 1) = 10^{300}$. The accuracy of this method is even in the vicinity of $k = 1$ comparable to the numerical accuracy and ranges, according to [47], in the order of 10^{-7}.

4.4 Discrete Potential Equations

To formulate the complete elliptical integrals in a discrete form the integrands of Eq. 4.8 and 4.14 are separated in a purely radius dependent and a surface density term. Furthermore, the integral boundaries need adjustment since the disk expands from the inner radius r_{in} to the outer radius r_{out}. Outside the disk boundaries the surface density is set to zero and thus the contributions to the potential vanish. As a consequence of the grid structure, the surface density has a constant value between two gridpoints. Therefore the integral can be written as a sum of integrals covering

two gridpoints. The potential of the disk at the gridpoint R_i is then

$$\begin{aligned}
\Phi(R_i) &= -2\mathrm{G}\int_0^{\infty} \Sigma(R_j) k K(k) \sqrt{\frac{R_j}{R_i}} dR_j \\
&= -2\mathrm{G}\int_{R_{in}}^{R_{out}} \Sigma(R_j) k K(k) \sqrt{\frac{R_j}{R_i}} dR_j \\
&= \sum_{j=1}^{np-1} \Sigma(R_j) \int_{R_j}^{R_{j+1}} -2\mathrm{G}\frac{\sqrt{R_j}}{\sqrt{R_i}} k K(k) dR_j \\
&= \sum_{j=1}^{np-1} \Sigma(R_j) \mathcal{I}_j \, .
\end{aligned} \tag{4.17}$$

Accordingly, the equation of the gradient writes

$$\begin{aligned}
\frac{\partial \Phi(R_i)}{\partial R} &= \frac{\mathrm{G}}{R_i^{\frac{3}{2}}} \int_0^{\infty} \Sigma(R_j) k \sqrt{R_j} \Big[K(k) - \frac{k^2}{1-k^2} \frac{E(k)}{4} \Big(- \frac{R_i}{R_j} + \frac{R_j}{R_i} + \frac{z^2}{R_i R_j} \Big) \Big] dR_j \\
&= \sum_{j=1}^{np-1} \Sigma(R_j) \int_{R_j}^{R_{j+1}} \frac{\mathrm{G}}{R_i^{\frac{3}{2}}} k \sqrt{R_j} \Big[K(k) - \frac{k^2}{1-k^2} \frac{E(k)}{4} \Big(- \frac{R_i}{R_j} + \frac{R_j}{R_i} + \frac{z^2}{R_i R_j} \Big) \Big] dR_j \\
&= \sum_{j=1}^{np-1} \Sigma(R_j) \mathcal{J}_j \, ,
\end{aligned} \tag{4.18}$$

where $\mathcal{I}$ and $\mathcal{J}$ are abbreviations for the integral expressions and np is the number of gridpoints. The problem of calculating the potential and its gradient has now been reduced to a summation and the integrals $\mathcal{I}$ and $\mathcal{J}$ can be evaluated by using a trapezoidal rule.

4.5 Numeric Implementation

After having written the gravitational potential and the gravitational force in continuous and discrete form, the respective expressions have to be implemented into the model, paying attention to the numerical properties of the TAPIR code. As a result of the 5-point-stencil at each gridpoint R_i, the potential (the gradient follows exactly

the same method) can be calculated as

$$\begin{aligned}\Phi(R_i) = \sum_{j<i-2} \Sigma_{j,old}\mathcal{I}_j + \Sigma_{i-2}\mathcal{I}_{i-2} + \Sigma_{i-1}\mathcal{I}_{i-1} + \Sigma_i\mathcal{I}_i \\ +\Sigma_{i+1}\mathcal{I}_{i+1} + \Sigma_{i+2}\mathcal{I}_{i+2} + \sum_{j>i+2} \Sigma_{j,old}\mathcal{I}_j \,,\end{aligned} \tag{4.19}$$

where $\Sigma_{\mathrm{j,old}}$ is the surface density at the previous timestep. As the gravitational potential is acting instantaneously, a change beyond the 5-point-stencil would also effect the potential at the gridpoint R_i. This effect however, reduces with distance and the combined change of all other gridpoints is negligible compared to the old timestep. Another problem arises when combining the potential with the adaptive grid. Using a fixed grid, the integrals $\mathcal{I}$ and $\mathcal{J}$ have to be calculated once prior to the first timestep. With an adaptive grid and changing the values of R_i, these integrals have to be updated at every timestep. Since the integrals require np^2 calculations, the computation time increases. Finally, the situation $R_i = R_j$ has to be discussed. In this case applies $k = 1$ and $K(k)$ approaches infinity. The resulting potential and its gradient would also diverge, which is not realistic. To reduce the impact of this problem, e.g. R_j could be slightly shifted so that $R_i \neq R_j$ is assured and thus does not result in a singularity.

4.6 Impact on the Vertical Structure

The gravitational potential of the disk does not only act in radial direction, the vertical direction is also affected. According to Eq. 1.10 and Eq.1.12, gravity contributes to the pressure scale height H_{p}. Additional to the stellar gravitational acceleration, the gravitational contribution of the disk has to be taken into account (similar to e.g. [5]). For a fixed radius and angle ($\partial_{\mathrm{r}} = \partial_\varphi = 0$) in cylindrical coordinates the Poisson equation (Eq. 4.1) reduces to

$$\frac{\partial^2\Phi}{\partial z^2} = 4\pi\mathrm{G}\rho\,. \tag{4.20}$$

Performing an integration over the vertical direction (analog to e.g. [43]) and using the symmetry of the disk and the definition of the surface density, Eq. 4.20 changes to

$$2\partial_z\Phi = 4\pi\mathrm{G}\Sigma\,. \tag{4.21}$$

The gravitational acceleration in vertical direction can be written as $g_z = -\partial_z \Phi$ and so the self gravity of the disk has a direct influence on the scale height of the disk since the g_z has to be added to the acceleration exerted by the central star. This changes Eq. 1.10 as follows:

$$\frac{dP}{dz} = -\rho \frac{GM_* z}{(r^2 + z^2)^{3/2}} - \rho g_z \,. \tag{4.22}$$

Ignoring the central star for now and using the equation for an ideal gas changes the hydrostatic equilibrium to

$$\frac{1}{\rho}\frac{d\rho}{dz} = -\frac{g_z}{e(\gamma - 1)} = -\frac{2\pi \mathrm{G}\Sigma}{e(\gamma - 1)} \,. \tag{4.23}$$

Now, caused by the self gravity of the disk, a scale height similar to Eq. 1.11 can be introduced

$$H_z = \sqrt{\frac{e(\gamma - 1)}{2\pi \mathrm{G}\Sigma}} \,. \tag{4.24}$$

The two expressions for the scale height (see Eq. 1.12) are acting simultaneously. They are combined using the harmonic mean (see e.g. [10])

$$H_{p,tot}^2 = \frac{1}{\frac{1}{H_z^2} + \frac{1}{H_p^2}} \,, \tag{4.25}$$

$$H_{p,tot} = \sqrt{\frac{e(\gamma - 1}{\mathrm{G}} \frac{1}{\frac{4\pi^2 \mathrm{G}\Sigma^2}{e(\gamma - 1)} + \frac{M_*}{r^3}}} \,. \tag{4.26}$$

The numerical implementation does not require additional steps since all the required variables are already defined in the TAPIR code.

4.7 Dominant Disk Self Gravity

The disk's self gravity is negligible for small disk masses. For increasing disk masses however, it impact increases as well. A critical point where the disk's gravity becomes dominant can be approximated according to [5]. Comparing the two gravitational acceleration terms in vertical direction at $z = H_p$, the disk's influence becomes dominant for

$$2\pi \mathrm{G}\Sigma > \frac{\mathrm{G}M_* H_p}{r^3} \,. \tag{4.27}$$

This can be rewritten into a criterion, at which self gravity of the disk becomes

important and has to be included in the simulation. Bringing all terms in Eq. 4.27 on one side and defining the respective value as the self gravity criterion Q_{SG} (similar to the Toomre parameter) yields

$$Q_{SG} \sim 1 > \frac{M_* H_P}{2\pi r^3 \Sigma} \ , \tag{4.28}$$

where Q_{SG} is of order 1. In Section 6 three different disks are compared. As the surface density decreases Q_{SG}, one low mass disk with $Q_{SG} > 1$, a critical disk with $Q_{SG} \sim 1$ and a high mass disk with $Q_{SG} < 1$ are tested.

4.8 Summary

In this chapter the potential of a protostellar disk is derived by rewriting the general solution of the Poisson equation with the help of the complete elliptic integral of the first kind. The physical interpretation of the complete elliptical integrals is the summing-up of all the parts of the symmetrical distribution of the disks surface density that contribute to the gravitational potential. Furthermore, the derivative with respect to the radius is calculated. These results are derived under the given assumptions for continuous functions of the surface density Σ and the elliptical integrals. Since Σ and the grid points, which represent the radius, are given in discrete distributions, the potential and the derivative have to be discretized as well. First, the complete elliptic integrals are calculated numerically using the AGM method. The resulting deviations to the analytic values are far below numerical accuracy. The potential is rewritten to a sum of integrals ranging over two gridpoints. Between two gridpoints the surface density is constant and so the problem of solving the integral is reduced towards a sum in which the remaining, only radius dependent integrals, can be calculated using the trapez method. This, however, increases the computational time especially if the gridpoints are moving since the radius dependent parts have to be calculated in every time step. Finally, the impact of the disk's potential on the vertical structure through the scale height is derived. By comparing the gravitational acceleration of the star and the disk, a criterion is formulated which should determine, when it is important to include the disk's self gravity to the simulation. In the next section some tests are performed to show the plausibility of the assumptions and the behaviour of the potential.

5 Tests

In this section, the equation for the potential of the protostellar disk is tested in different ways. First, the gravitational potential energy of the young solar system will be compared from different points of view. The mass conservation and the related conservation of the total potential is then verified using the discrete equation of the potential (Eq. 4.17) in a numeric test case. Afterwards, the implementation is tested by increasing the disk's density at a specific point in the disk and analysing the behaviour of the potential on the density evolution.

5.1 Comparing Gravitational Potential Energy

To test the analytic potential function $\Phi(R)$ of the disk the gravitational potential energy U of the system will be calculated. First, the mass of the star which is concentrated at radius zero is placed within the disk's potential. The result is then compared to the mass of the disk placed in the stars potential. At radius zero Eq. 4.8 changes to

$$\Phi(0) = -4\mathrm{G} \int_{R_{in}}^{R_{out}} \Sigma(R')K(0)dR' \,. \tag{5.1}$$

With $K(0) = \pi/2$ the gravitational energy can be calculated as

$$U = \int M_* d\Phi(0) = -2\pi\mathrm{G}M_* \int_{R_{in}}^{R_{out}} \Sigma(R')dR' \,. \tag{5.2}$$

Expanding this equation with R' one ends up with

$$U = -\int_{R_{in}}^{R_{out}} 2\pi R'\Sigma(R')\frac{GM_*}{R'}dR' = \int \Phi_* dM_D \,, \tag{5.3}$$

which represents the mass of the disk placed in the stars potential. Thus, the gravitational potential energy is independent of the point of view.

5.2 Conservation of Mass

The following test considers the numeric discretization and verifies the conservation of the total potential. Since the potential of a protostellar disk is up to three orders of magnitude smaller compared to the potential of the star, a system will be constructed in which the initial mass of the disk equals the initial mass of the star. Thus the potential will have the same order of magnitude. The initial mass is set to unity. During an arbitrary time $T = 1$, the complete mass from the disk falls onto the star

which doubles the amount of stellar mass at the end of the simulation. The total potential Φ_{tot} of the system is the sum of the disk and stellar potential. Since the mass of the system is conserved, integrating the potential over the radius should result in the same value for all timesteps t

$$\int \Phi_{\rm tot} dR = \text{const } \forall t \, . \tag{5.4}$$

Since gravity is a long ranging force this integral has to be evaluated from zero to infinity. This is only possible analytically. For this numerical test the outer boundary R_∞ is chosen to be three orders of magnitude larger than the outer radius of the disk. The stellar radius equals the inner radius of the disk $R_* = R_{in} = 0.1$ and the outer radius of the disk $R_{out} = 2$ and $R_\infty = 2000$ respectively. To calculated the potential of the disk, the domain is divided into three parts. In each part 400 gridpoints are used. The first part ranges from zero to the inner radius of the disk; the second part from the inner to the outer radius of the disk and the third part from the outer edge of the disk to R_∞. In each part the potential is calculated according to Eq. 4.17. The star's potential can be split in two parts. From zero to the stellar radius the formula for a homogeneous sphere

$$\Phi(R)_{*,in} = \frac{\mathrm{G}M_*}{2R_*} \left(R^2 - 3R_*^2\right) \tag{5.5}$$

and from the stellar radius to R_∞, $\Phi(R)_{*,out} = -GM_*/R$ is used. The integral over the stars potential can be calculated analytically. In Fig. 6 the result for a disk with a constant surface density is shown. The integrated potential of the disk (solid line) and the star (dashed line) as well as the total integrated potential (dotted line) are calculated for 200 timesteps. Since the disk-mass is added onto the star, the disk's potential decreases and the stellar potential increases. The total value remains nearly constant. The maximum difference in the total potential is 0.3% and decreases for a lower disk-mass. Keeping in mind that the actual disk-mass is only a small fraction of the stellar mass, the error will even be smaller in more realistic systems. This test shows, that the numeric method is compatible with the conservation of the total potential of the system and provides accurate results.
The accuracy depends on the number of gridpoints and especially on the value of R_∞. For smaller values of R_∞ the accuracy decreases. Indeed, the maximum deviation for $R_\infty = 1000$ is $\sim 5\%$ and $\sim 7\%$ for $R_\infty = 50$.

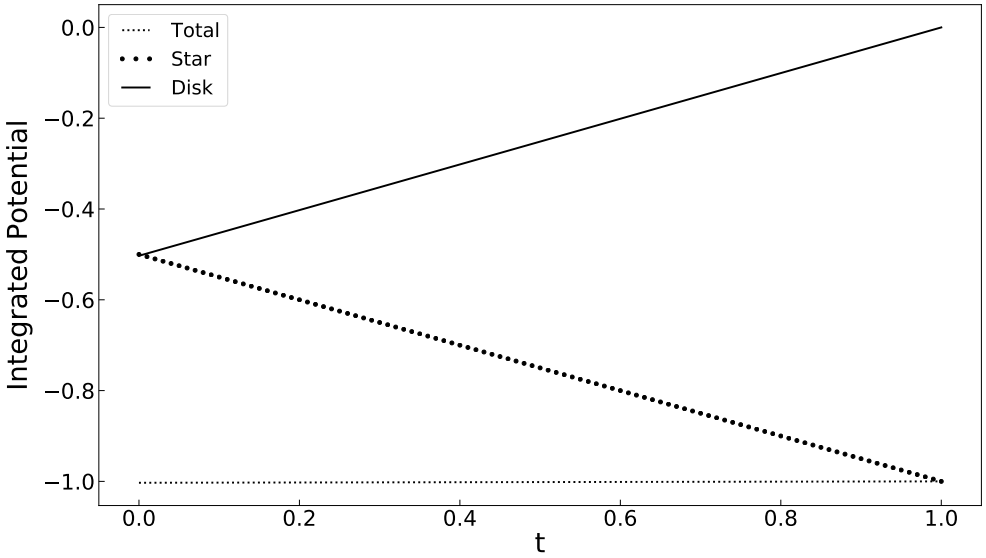

Figure 6: Different potential functions integrated over an arbitrary time t and normalised to the integrated total potential (Total). The integrated potentials of the disk (Disk) and the star (Star) are shown. They were calculated in 200 timesteps.

5.3 Adding Mass to the disk

For this test the initial model of a protoplanetary disk around a $1M_{\odot}$ star constructed. The idea is to add the mass of a Jupiter at an arbitrary radius r_{ref} by increasing the surface density and follow the evolution of this perturbation. The potential of the disk is expected to show a gravitational cavity at r_{ref}. Viscous forces then transport the mass away from the cavity, both inwards and outwards. This widens the mass accumulation and the potential cavity until the mass is evenly distributed along the disk. This process is visible in Fig. 7. The temporal progress of this process is shown at four evolution ages, starting with the initial disk τ_0 without the mass injection, the time after the mass injection τ_1 and two more times showing the progress until the entire mass is redistributed (τ_2 and τ_3). The peak in the surface density, the gravitational cavity in the potential and the cavity's widening is clearly visible.

5.4 Known Limitation

Since gravity is a long-ranged force and changes in the potential function appear instantaneously within the gravitational field, numerical limitations occur. The TAPIR code uses a five-point stencil, only at these points the variables are calculated for the new time step. To overcome this issue, the old values are taken into account for the

remaining gridpoints. Gravitational force however, is decreasing fast with increasing distance. Even if there are mass shifts beyond the five-point stencil, gravity shifts are reduced and differences to the old timestep are marginal.

5.5 Summary

The gravitational energy as well as the conservation of the total mass shows satisfactory results during these tests. Furthermore, the effects of a mass added onto the disk at a given radius is reproduced realistically. Moreover, the limitations regarding the gravitational force have been discussed. Since all tests show satisfying results, the impact of the potential on more realistic disks is shown in the next section.

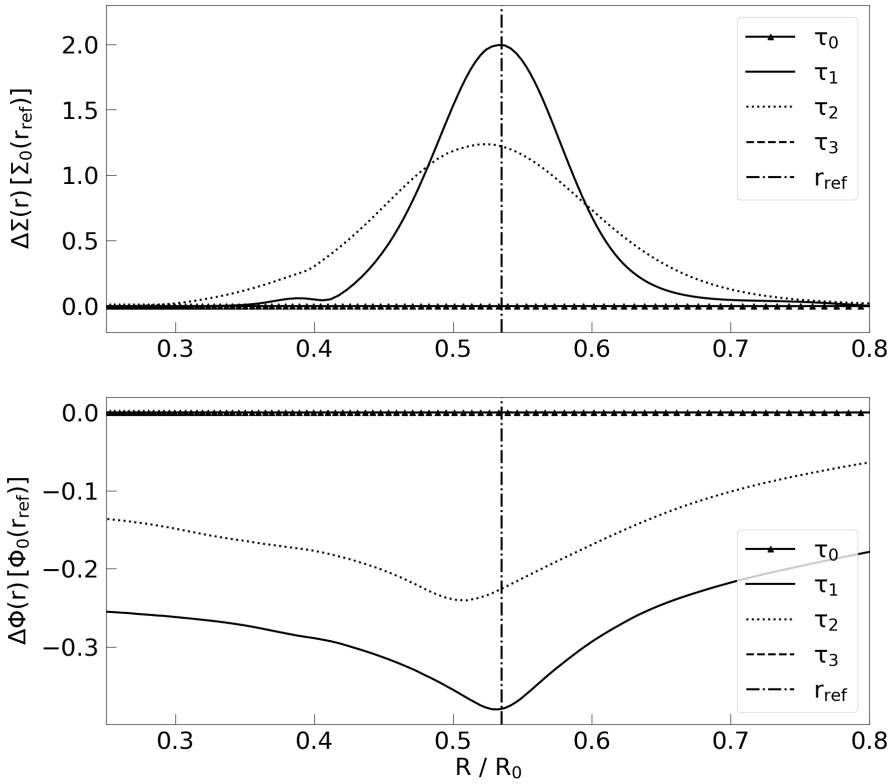

Figure 7: Upper panel: Surface density distribution after a mass increase at a radius r_{ref} during different timesteps. τ_0 represents the initial density prior the mass injection; τ_1 shows the distribution directly after the increase and τ_2 as well as τ_3 show the further progress. All distributions are normalised to the value of the initial density distribution (τ_0) at r_{ref}. Lower panel: Respective illustration of the disk's gravitational potential. The plots are normed to the initial potential at r_{ref}. (see [38])

6 Results

In this section the profile and temporal evolution of different protoplanetary disks is tested under the influence of the gravitational potential of the disk. After a short excursus introducing episodic accretion events, a complete temporal evolution of a disk with and without the disk's potential will be compared for different values of Q_{SG}. Finally, the influence of an episodic accretion event (FU Orionis like outburst, see e.g. [6] or [9]) on Q_{SG} is tested.

6.1 Episodic Outburst Events

The basis of accretion outbursts as described in e.g. [6] or [9] is the layered viscosity model as introduced in Section 2.4. Accreting layers at the boundary of the disk enclose a part of cool gas. The temperature of this locked gas is first of all too low to trigger MRI turbulence. As this gas cannot be transported efficiently in radial direction ([7]), more and more material is accreted into this region the temperature increases until it reaches the critical value of T_{crit}. In this case turbulence induced and the zone of former cold gas falls onto the star increasing the accretion rate from $\dot{M} \sim 10^{-8} M_{\odot}/\mathrm{yr}$ to $10^{-6} - 10^{-5} M_{\odot}/\mathrm{yr}$ (see e.g. [6]). This increases the temperature even further and an instability starts until the gas is depleted and the temperature decreases below the critical value. The reason why these events are interesting in this context are the waves, which are triggered with the outburst and move through the disk. Together with the waves masses within the disk are shifted and so a local increase of the importance of the disk's potential compared to the stellar potential could occur.

6.2 Different values of $\mathrm{Q_{SG}}$

To show the influence of self gravity for different values of Q_{SG} (Eq. 4.28), the same disk and stellar parameters are used for all runs. The star is a solar like star with $1 M_{\odot}$ and the disk ranges from 0.06 to 30 AU. The viscosity parameter alpha is set to be constant; $\alpha = 0.01$. The effect of a layered viscosity model and the resulting outbursts are shown in the next subsection. For each disk mass a run with and without the gravitational influence of the disk is made. Then the disk structure of the initial, stationary model (in this case the surface density profile and the scale height with respect to the radius) as well as the temporal evolution (the disk mass and the accretion rate onto the star) are compared.

6.2.1 Low Mass Disks

First, we show the influence of the disk potential on the disk structure, for a low-mass disk. The disk mass is $\sim 1\% M_*$ which corresponds to the MMSN [24]. The parameter Q_{SG} has a value of ~ 7. In Fig. 8 and 9 can be seen that the inclusion of the potential does not change the structure of the disk noticeable. The surface density as well as the scale height are unaffected over the whole range of the disk radius. The temporal evolution of the low mass disk looks similar. In Fig. 10 minimum deviations can be guessed during an early phase of the disk lifetime. The accretion rate again is quasi undisturbed during the whole evolution (see Fig. 11).

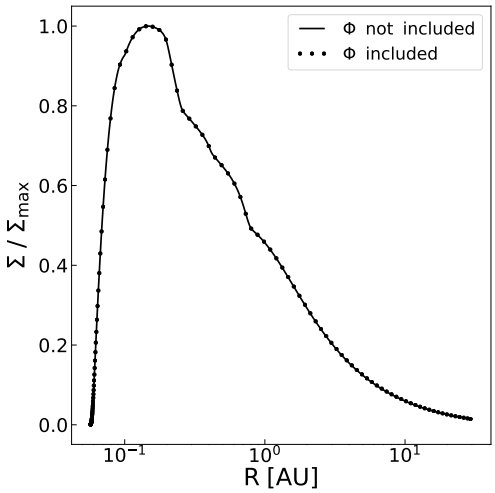

Figure 8: Low-mass disk. Surface density Σ of the disk with respect to the radius R. The radius is given in AU and the surface density is normed to the maximum value. The *dots* represent the simulation in which the gravitational potential of the disk is included. The *line* shows the run without the disk's potential.

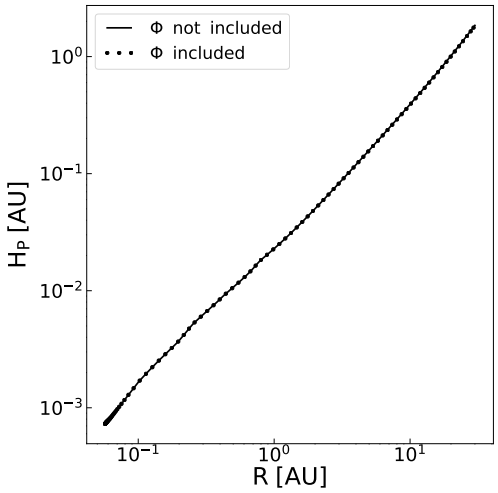

Figure 9: Low-mass disk. Scale height of the disk H_p as a function of the radius R. The radius and the scale height is given in AU. The *dots* represent the simulation in which the gravitational potential of the disk is included. The *line* shows the run without the disk's potential.

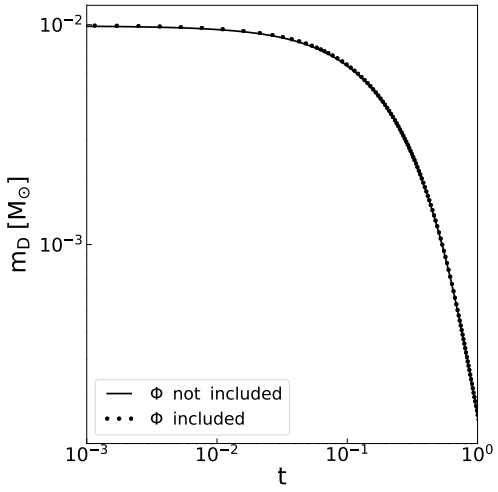

Figure 10: Low-mass disk. Disk mass m_D in solar mass units as a function of the simulation time t in units of the maximum value t_max. The *dots* represent the simulation in which the gravitational potential of the disk is included. The *line* shows the run without the disk's potential.

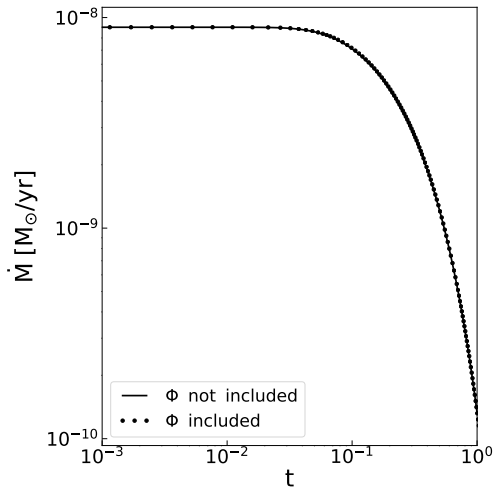

Figure 11: Low-mass disk. Disk accretion rate onto the star $\dot{M}$ in solar masses per year as a function of the simulation time t in units of the maximum value $t_{\max}$. The *dots* represent the simulation in which the gravitational potential of the disk is included. The *line* shows the run without the disk's potential.

6.2.2 Critical Disks

In the second run a disk with a larger mass is simulated ($\sim 5\% M_*$). The parameter Q_{SG} has a minimum value of ~ 1.5. This is close to 1 and thus the gravitational potential of the disk should already have an impact on the disk. This however is expected to make a difference in the outer parts of the disk, since the Eq. 4.28 decreases with increasing radius. With the approximation for H_P used for Eq. 1.13 as well as the dependency for Σ used in the MMSN [24], Q_{SG} goes with $r^{-1/4}$. Indeed a change in the outer regions of the surface density as well as in the scale height can be seen (see Fig. 12 and 13). During the evolution of the disk, there are bigger changes than before (see Fig. 14 and 15) but these changes are still small and the different runs are still comparable in their structure.

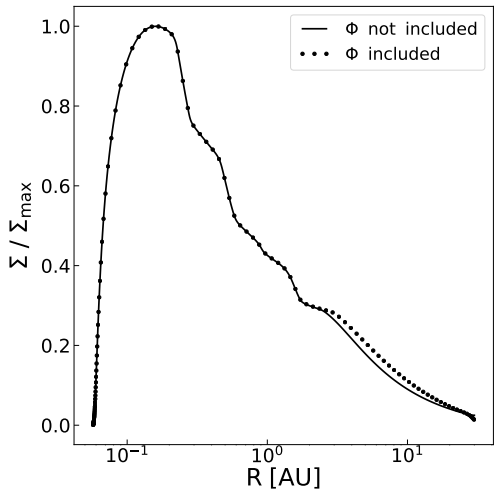

Figure 12: Critical-mass disk. Surface density Σ of the disk with respect to the radius R. The radius is given in AU and the surface density is normed to the maximum value. The *dots* represent the simulation in which the gravitational potential of the disk is included. The *line* shows the run without the disk's potential.

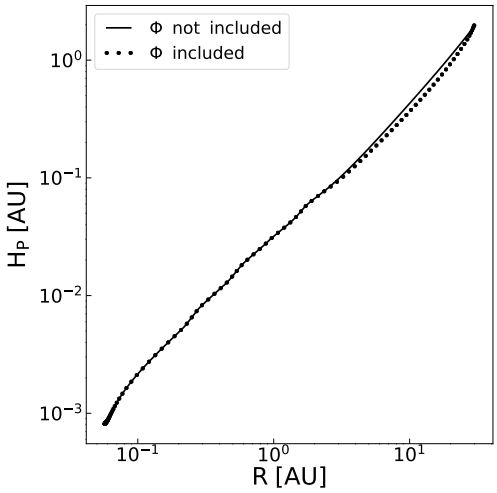

Figure 13: Critical-mass disk. Scale height of the disk $H_{\rm p}$ as a function of the radius R. The radius and the scale height is given in AU. The *dots* represent the simulation in which the gravitational potential of the disk is included. The *line* shows the run without the disk's potential.

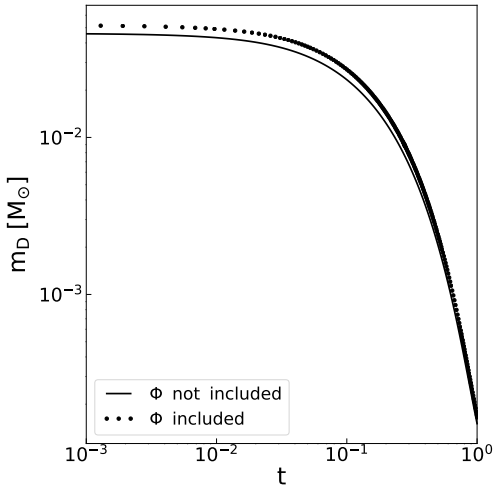

Figure 14: Critical-mass disk. Disk mass m_D in solar mass units as a function of the simulation time t in units of the maximum value $t_{\rm max}$. The *dots* represent the simulation in which the gravitational potential of the disk is included. The *line* shows the run without the disk's potential.

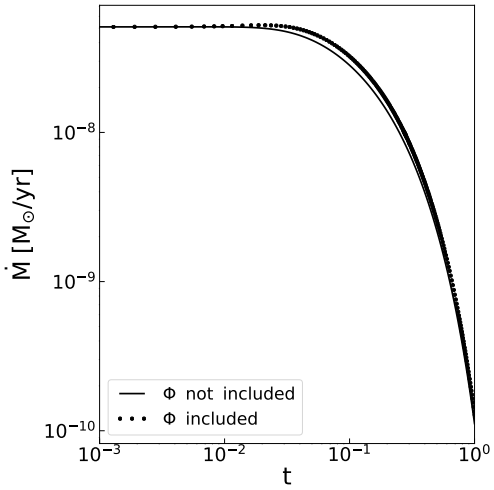

Figure 15: Critical-mass disk. Disk accretion rate onto the star $\dot{M}$ in solar masses per year as a function of the simulation time t in units of the maximum value $t_{\max}$. The *dots* represent the simulation in which the gravitational potential of the disk is included. The *line* shows the run without the disk's potential.

6.2.3 High Mass Disks

In the third run a heavy disk is simulated ($\sim 10\% M_*$). The parameter Q_{SG} has a minimum value of ~ 0.7. This is already in the range where the disk self gravity should be dominant and a significant change should be noticeable. This change should again be strongest in the outer parts of the disk. As expected there is a tremendous change in the surface density profile in Fig. 16 as well as in the scale height in Fig. 17. This effect in the stationary model can be explained as follows: The scale height is decreased due to the increased combined value of acceleration towards the central plane of the disk as seen in Fig. 17. Thereby the angle at which the disk is illuminated by the star decreases as well. So the temperature is reduced due to this shadowing effect. These two effects, the lower scale height and the shadowing, both influence the viscosity value $\nu = \alpha c_s H_P$. The scale height reduces ν directly and the lower temperature decreases the speed of sound c_s and thus also decreases ν. Since according to e.g. [5] the following for a stationary disk is true: $\dot{M} = \nu\Sigma = const$, the surface density has to increase to fulfil this condition. This higher surface density in the other parts increases the disk mass significantly (as seen in Fig. 18) and so the temporal evolution of the disk is affected as well. The accretion rate in Fig. 19 is even qualitative different. The higher mass of the initial model results in an initial increase of the accretion rate onto the star.

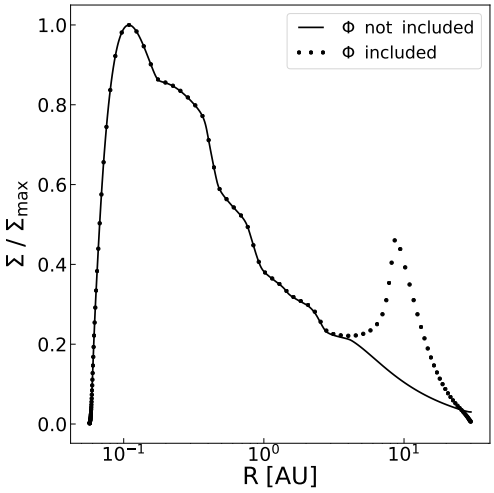

Figure 16: High-mass disk. Surface density Σ of the disk with respect to the radius R. The radius is given in AU and the surface density is normed to the maximum value. The *dots* represent the simulation in which the gravitational potential of the disk is included. The *line* shows the run without the disk's potential.

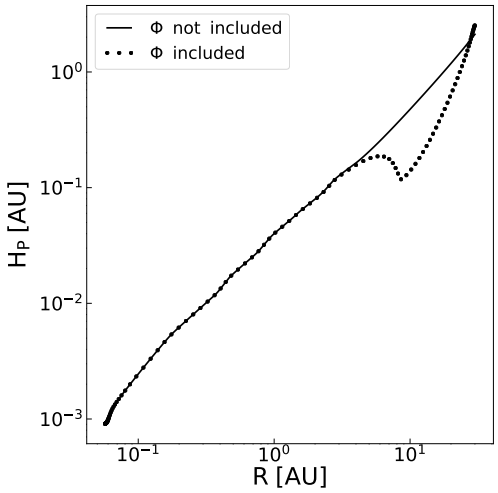

Figure 17: High-mass disk. Scale height of the disk H_p as a function of the radius R. The radius and the scale height is given in AU. The *dots* represent the simulation in which the gravitational potential of the disk is included. The *line* shows the run without the disk's potential.

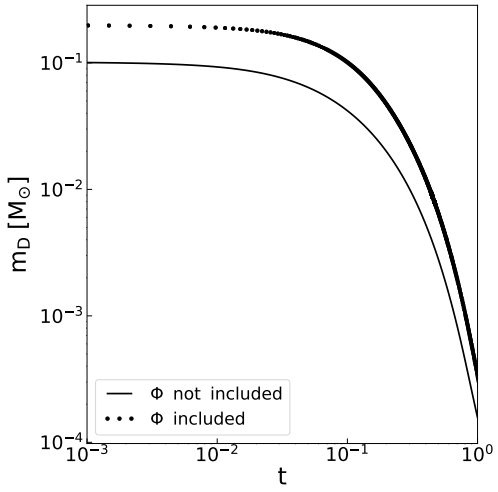

Figure 18: High-mass disk. Disk mass m_D in solar mass units as a function of the simulation time t in units of the maximum value t_max. The *dots* represent the simulation in which the gravitational potential of the disk is included. The *line* shows the run without the disk's potential.

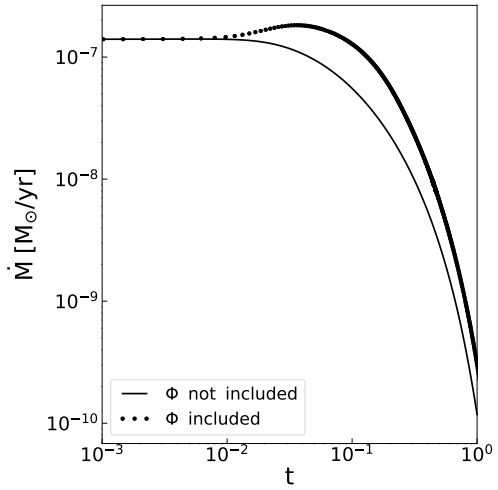

Figure 19: High-mass disk. Disk accretion rate onto the star $\dot{M}$ in solar masses per year as a function of the simulation time t in units of the maximum value $t_{\max}$. The *dots* represent the simulation in which the gravitational potential of the disk is included. The *line* shows the run without the disk's potential.

6.3 Impact of episodic accretion events on $\mathrm{Q_{SG}}$

In the previous section the different simulations are carried out with a constant value for the viscosity parameter α. Now the effect of a layered accretion and the resulting outbursts are tested. For this purpose a low mass disk is simulated ($Q_{SG} \sim 20$). In Fig. 20 the accretion rate during the burst as well as the value for Q_{SG} can be seen. Q_{SG} is normed to its initial value of ~ 20. It can be seen, that as soon as the outburst starts, Q_{SG} increases and thus decreases the influence of the disk's self gravity. As the burst fades Q_{SG} remains even above its initial value. Concluding from this results, an episodic accretion event like an FU Orionis like outburst, does not increases the effect of the disk's self gravity, on the contrary it is reduced. This effect can be explained by the rapid and strong increase in the disks temperature during these events (see e.g. [6] or [9]).

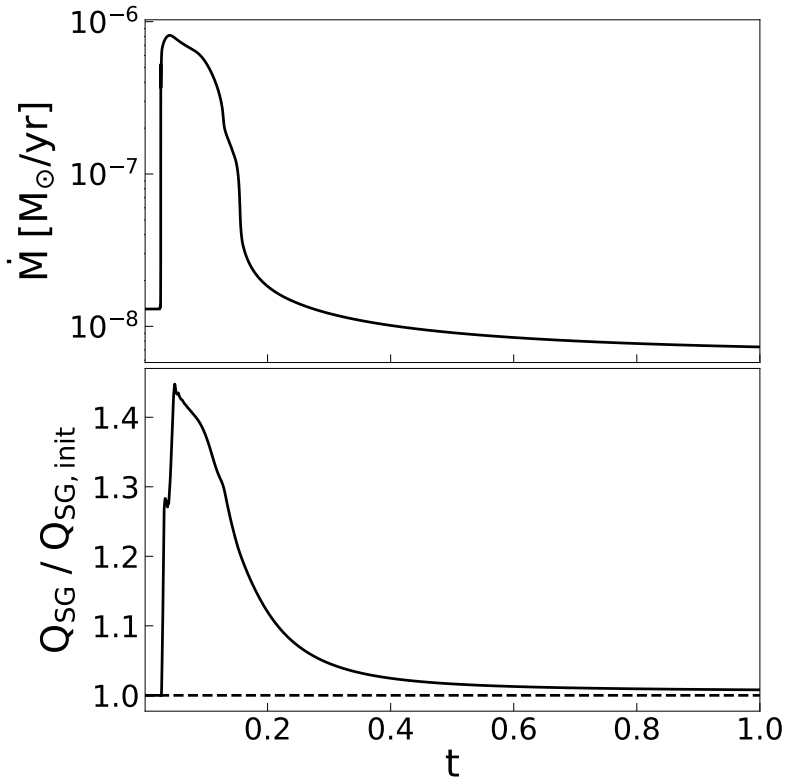

Figure 20: Upper panel: Accretion rate in solar masses per year. Lower panel: Value of Q_{SG} in units of $Q_{\mathrm{SG,\,init}}$. Both are given in units of the time; ranging over the duration of the burst and normalised to its final value.

6.4 Summary

In this section the results are presented. First, episodic accretion events were briefly explained and the reason for their consideration stated. Afterwards different values of Q_{SG} are tested and the impact of the disk's self gravity illustrated in both the stationary model of the disk as well as in the temporal evolution. Finally, the impact of episodic accretion outbursts on the parameter Q_{SG} is shown. As this section completes the separate parts of this work, the next section gives a conclusion of these results.

7 Conclusion

In this work the implicit TAPIR code is introduced, its key features addressed and the physical and the temporal dimensions of a protoplanetary disk are estimated. Subsequently, the equations and the numerical methods used are explained. Since these parts should act as a review, the respective references are given for deeper insights. Thereafter, the gravitational potential and its gradient of the disk are calculated, using complete elliptical integrals. This method is chosen since these integrals can be easily calculated numerically up to sufficient accuracy. With the discrete form of the elliptic integrals, the implementation of the potential's gradient into the equation of motion is carried out by rewriting the potential as a finite sum. Unfortunately, this implementation increases the computation time. Especially if the gridpoints are moving and the parts depending on the gridpoints have to be calculated in every timestep. Additionally, the impact in the radial equation of motion, the impact of the potential is also implemented in the pressure scale height. Comparing the gravitational acceleration of the star and the disk, a criterion Q_{SG} is derived which can determine when the disk gravity become important. For value of Q_{SG} close to unity the impact of the disk's gravity should become important. In the following tests to check the correct implementation the potential shows satisfactory results. Furthermore, three different simulation runs for disks with different values of Q_{SG} are compared with and without the influence of the disk gravitational potential. For low-mass disks ($Q_{\mathrm{SG}} > 1$) the effect is not noticeable. Increasing the disk mass and decreasing Q_{SG} to approximate unity the effects increase but remain still small and the qualitative structure and evolution remains the same. For even heavier disks ($Q_{SG} < 1$) the impact of the disk's gravity becomes dominant in the outer parts of the disk, resulting in distinct changes in the disk structure and the temporal evolution. Finally, the impact of episodic accretion events on Q_{SG} is tested. A comparison of Q_{SG} over the course of such an outburst event shows, that Q_{SG} increases due to the strong temperature rise during an outburst. This reduces the effect of the disk's gravity.

Combining these results, it is absolutely reasonable to ignore the disk's self gravity for low-mass disks. The structure and the evolution of the disk remain almost unchanged when adding the potential into the model. Even if the value of Q_{SG} approaches unity the differences are sill not qualitative. For higher disk masses ($Q_{\mathrm{SG}} < 1$) however, the impact is significant and the inclusion of the gravitational potential of the disk should be considered. Ignoring the gravitational effects for high-mass disks can lead to substantial deviations in both the disk structure and evolution.

Further Outlook

The TAPIR code is constantly expanded with new features. There are features, that are already implemented in the model, but not yet fully analysed. These, as well as further tests with the existing model, could change the results of this work and give new insights on protoplanetary disks.

One included aspect in the current model is the efficiency of the accretion process, which is divided in three factors. First, the efficiency of the mass accretion f_{acc} can be varied. Describing how much of the accreted mass is added onto the star. And how much mass is lost in stellar winds. Furthermore, the change of the stellar irradiation efficiency f_{irr} (see Eq. 2.35), can be changed. The higher f_{irr}, the more radiation is absorbed from the disk and less energy is reflected. The third efficiency parameter describes the accretion luminosity f_{lum}. Higher f_{lum} leads more energy of the accreted material to be converted into stellar luminosity. In addition, the properties of the gas within the disk itself can be adapted. The equation of state can be changed from a perfect gas with a mean molecular weight of 2.33 g/mol to a more realistic gas, which has to be given in tables. To adjust for different metallicities Z, opacity tables for different Z values can be used. A collection of opacities from different authors and for different metallicities can be found here [1].

Besides the further analysis of the existing model, several new features are being implemented into the model. One possibility is the treatment of stellar jets. According to e.g. [18], jets are found originating from young stellar objects. As a consequence, the disk is not only irradiated by the star itself, but also by a jet, releasing energy onto the disk's surface. This energy input also contributes to the energy transport in vertical direction. As the material in the jet is moving away from the star, the intensity of the radiation and the angle under which the disk is irradiated changes. Another aspect, which is currently being implemented into the TAPIR code, is a planet-disk interaction. A single planet, orbiting the central star, can have a large impact on the protoplanetary disk. The planet's mass attracts the disk material in its vicinity and a gap within the disk can open (see e.g. [5] Fig. 32 and references therein). As the current model utilizes 1-D calculations and axial-symmetry, a single planet orbiting the central star is difficult to implement. A sinkterm, however, implemented at a given radius, can represent at least the gravitational presence of a planet embedded in the disk (keeping in mind, that a sinkterm does not represent the physics of a whole planet). In the current model, the effects of the stellar magnetic field are limited towards the inner regions of the disk and the truncation radius. It

is possible to add a large-scale, primordial disk magnetic field to the model, effecting the disk over its whole radial range and being the reason for e.g. disk winds. I want to finish this outlook with one more additional extension to the model; the enhanced treatment of dust. In the current model, a constant dust-to-gas ratio of 0.01 is used. In recent publications (e.g. [45]) however, this ratio can differ from the constant value significantly (values up to 1). In regions of a high dust-to-gas ratio, the increased optical depth due to the dust causes more efficient radiative heating within the disk, which then has a influence on the viscous parameters. As the viscosity is directly influenced by the surface density (see Sec. 6.2.3), the whole disk structure is effected. Additionally, dust-settling, dust-growing, fragmentation and different drag-regimes have to be distinguished.

Despite the work left to be done, the current model is able to reproduce previous work on protoplanetary disks (see [38]) in a satisfactory manner. Furthermore, the implicit nature of the TAPIR code enables long term simulations (as shown in Sec. 6.2), which have been not possible with the given accuracy so far (especially towards the inner regions of a disk). One example of such a case is the upper mass limit due to viscous instabilities for stationary protoplanetary accretion disks [39].

Acknowledgement

I especially want to thank Florian Ragossnig, Ernst Dorfi and Daniel Steiner for helpful advice, lively discussions, occasional pushes in the right directions and of course a lot of patience.

A Appendix

A.1 Detailed calculation of equation 4.4

With $\vec{x} = (R, \phi, z)$ and $\vec{x}' = (R', \phi', 0)$.

$$\begin{aligned} |\vec{x} - \vec{x}'|^2 &= R^2 + R'^2 - 2RR'\cos(\phi') + z^2 \\ &= [(R+R')^2 + z^2]\frac{[R^2 + R'^2 - 2RR'\cos(\phi') + z^2]}{(R+R')^2 + z^2} \\ &= [(R+R')^2 + z^2]\left[1 - \frac{2RR'}{(R+R')^2 + z^2}(1 + \cos(\phi'))\right], \end{aligned} \tag{A.1}$$

using $(1 + \cos(\phi')) = 2\cos^2(\frac{1}{2}\phi')$ and $k^2 = 4RR'/((R+R')^2 + z^2)$:

$$\begin{aligned} &[(R+R')^2 + z^2]\left[1 - \frac{2RR'}{(R+R')^2 + z^2}(1 + \cos(\phi'))\right] \\ &= [(R+R')^2 + z^2][1 - \frac{4RR'}{(R+R')^2 + z^2}\cos^2(\frac{1}{2}\phi')] \\ &= [(R+R')^2 + z^2][1 - k^2\cos^2(\frac{1}{2}\phi')]\,. \end{aligned} \tag{A.2}$$

A.2 Substitution in equation 4.5

Using the following substitution $t = \cos(\frac{1}{2}\phi')$ and $d\phi' = \frac{-2dt}{\sin(\frac{1}{2}\phi')}$ with the new lower integral boundary 1 and upper boundary -1 and the relation $\sin(\frac{1}{2}\phi') = \sqrt{1-t^2}$

$$\begin{aligned} &\int_0^{2\pi} \frac{1}{\sqrt{1 - k^2\cos^2(\frac{1}{2}\phi')}} d\phi' \\ &= -2\int_1^{-1} \frac{1}{\sqrt{1-k^2t^2}\sqrt{1-t^2}} dt \\ &= 2\int_{-1}^{1} \frac{1}{\sqrt{1-t^2}\sqrt{1-k^2t^2}} dt\,. \end{aligned} \tag{A.3}$$

In the last step, the integral boundaries are switched changing the sign of the integral.

A.3 Complete elliptic integrals of the first and second kind

The complete elliptic integral of the first kind is defined as (e.g. [2])

$$K(k) = \int_0^1 \frac{1}{\sqrt{1-t^2}\sqrt{1-k^2t^2}} dt\,. \tag{A.4}$$

The complete elliptic integral of the second kind is defined as

$$E(k) = \int_0^1 \frac{\sqrt{1-k^2t^2}}{\sqrt{1-t^2}} dt\,. \tag{A.5}$$

Derivation of the complete elliptic integral of the first kind with respect to k

$$\begin{aligned} \frac{d}{dk}\Big(kK(k)\Big) &= K(k) + k\frac{dK(k)}{dk} \\ &\stackrel{!}{=} \frac{E(k)}{1-k^2}\,. \end{aligned} \tag{A.6}$$

Rewriting this equation with $K'(k)$ which represents the derivation of $K(k)$ with respect to k yields

$$k(1-k^2)K'(k) - E(k) + (1-k^2)K(k) \stackrel{!}{=} 0 \tag{A.7}$$

To prove this relation the definitions of the integrals are used as well as the following derivative

$$\frac{d}{dk}\left(\frac{1}{\sqrt{1-k^2t^2}}\right) = \frac{t^2k}{(1-k^2t^2)^{\frac{3}{2}}} \tag{A.8}$$

$$\begin{aligned} & k(1-k^2)K'(k) - E(k) + (1-k^2)K(k) \\ &= \int_0^1 dt\left[\frac{k(1-k^2)t^2k}{(1-k^2t^2)^{\frac{3}{2}}(1-t^2)^{\frac{1}{2}}} - \frac{(1-k^2t^2)^{\frac{1}{2}}}{(1-t^2)^{\frac{1}{2}}} + \frac{(1-k^2)}{(1-t^2)^{\frac{1}{2}}(1-k^2t^2)^{\frac{1}{2}}}\right] \\ &= \int_0^1 dt\left[\frac{k(1-k^2)t^2k - (1-k^2t^2)^2 + (1-k^2)(1-k^2t^2)}{(1-k^2t^2)^{\frac{3}{2}}(1-t^2)^{\frac{1}{2}}}\right] \\ &= -k^2\int_0^1 dt \frac{1+2t^2-k^2t^4}{(1-k^2t^2)^{\frac{3}{2}}(1-t^2)^{\frac{1}{2}}} \\ &= -k^2\int_0^1 dt \frac{d}{dt}\left(\frac{t(1-t^2)^{\frac{1}{2}}}{(1-k^2t^2)^{\frac{1}{2}}}\right) \end{aligned} \tag{A.9}$$

$$= -k^2\left[\left(\frac{t(1-t^2)^{\frac{1}{2}}}{(1-k^2t^2)^{\frac{1}{2}}}\right)\Big|_{t=1} - \left(\frac{t(1-t^2)^{\frac{1}{2}}}{(1-k^2t^2)^{\frac{1}{2}}}\right)\Big|_{t=0}\right] \qquad (A.10)$$
$$= -k^2(0-0) = 0$$

A.4 Derivative of k

With the definition of $k = \sqrt{4RR'/((R+R')^2+z^2)}$ the following derivative can be calculated

$$\begin{aligned}\frac{d}{dR}k &= \frac{d}{dR}\left(\frac{\sqrt{4RR'}}{\sqrt{(R+R')^2+z^2}}\right)\\ &= \frac{R'(R^2+R'^2+2RR'+z^2)-2R^2R'-2RR'^2}{(RR')^{\frac{1}{2}}((R+R')^2+z^2)^{\frac{3}{2}}}\\ &= \frac{R'^3+R'z^2-R^2R'}{(RR')^{\frac{1}{2}}((R+R')^2+z^2)^{\frac{3}{2}}}\\ &= \frac{R'(-R^2+R'^2+z^2)}{(RR')^{\frac{1}{2}}((R+R')^2+z^2)^{\frac{3}{2}}}\,.\end{aligned} \qquad (A.11)$$

This expression changes after multiplying a factor $2R$ (according to equation 4.11) to

$$\begin{aligned}2R\frac{d}{dR}k &= \frac{2RR'(-R^2+R'^2+z^2)}{(RR')^{\frac{1}{2}}((R+R')^2+z^2)^{\frac{3}{2}}}\\ &= \frac{k^3}{4}\left(-\frac{R^2}{RR'}+\frac{R'^2}{RR'}+\frac{z^2}{RR'}\right)\\ &= \frac{k^3}{4}\left(-\frac{R}{R'}+\frac{R'}{R}+\frac{z^2}{RR'}\right).\end{aligned} \qquad (A.12)$$

List of Figures

List of Tables

References

[1] Wsu low temperature opacities. `https://www.wichita.edu/academics/fairmount_college_of_liberal_arts_and_sciences/physics/Research/opacity.php`. Accessed: 2020-06-24.

[2] Abramowitz, M., and Stegun, I. A. *Handbook of mathematical functions : with formulas, graphs, and mathematical tables*. 1970.

[3] Andrews, S. M., Huang, J., Pérez, L. M., Isella, A., Dullemond, C. P., Kurtovic, N. T., Guzmán, V. V., Carpenter, J. M., Wilner, D. J., Zhang, S., Zhu, Z., Birnstiel, T., Bai, X.-N., Benisty, M., Hughes, A. M., Öberg, K. I., and Ricci, L. The Disk Substructures at High Angular Resolution Project (DSHARP). I. Motivation, Sample, Calibration, and Overview. *APJl 869* (Dec. 2018), L41.

[4] Armitage, P. J. *Astrophysics of Planet Formation*. 2010.

[5] Armitage, P. J. Physical processes in protoplanetary disks. *arXiv e-prints* (Sept. 2015), arXiv:1509.06382.

[6] Armitage, P. J., Livio, M., and Pringle, J. E. Episodic accretion in magnetically layered protoplanetary discs. *Monthly Notices of the Royal Astronomical Society 324*, 3 (06 2001), 705–711.

[7] Armitage, P. J., Livio, M., and Pringle, J. E. Episodic accretion in magnetically layered protoplanetary discs. *MNRAS 324*, 3 (June 2001), 705–711.

[8] Balbus, S. A., and Hawley, J. F. A Powerful Local Shear Instability in Weakly Magnetized Disks. I. Linear Analysis. *APJ 376* (July 1991), 214.

[9] Bell, K. R., and Lin, D. N. C. Using FU Orionis Outbursts to Constrain Self-regulated Protostellar Disk Models. *APJ 427* (June 1994), 987.

[10] Benítez-Llambay, A., Navarro, J. F., Frenk, C. S., and Ludlow, A. D. The vertical structure of gaseous galaxy discs in cold dark matter haloes. *473*, 1 (Jan. 2018), 1019–1037.

[11] Binney, J., and Tremaine, S. *Galactic dynamics*. 1987.

[12] Camenzind, M. Magnetized Disk-Winds and the Origin of Bipolar Outflows. In *Reviews in Modern Astronomy* (1990), G. Klare, Ed., vol. 3 of *Reviews in Modern Astronomy*, pp. 234–265.

[13] Caramana, E. J., Shashkov, M. J., and Whalen, P. P. Formulations of Artificial Viscosity for Multi-dimensional Shock Wave Computations. *Journal of Computational Physics 144* (July 1998), 70–97.

[14] Courant, R., Friedrichs, K., and Lewy, H. Über die partiellen Differenzengleichungen der mathematischen Physik. *Mathematische Annalen 100* (1928), 32–74.

[15] Dorfi, E. A. Radiation hydrodynamics: Numerical aspects and applications. In *Computational Methods for Astrophysical Fluid Row*. Springer Verlag, 1998, pp. 263–342.

[16] Dorfi, E. A., and Drury, L. O. Simple adaptive grids for 1-D initial value problems. *Journal of Computational Physics 69* (Mar. 1987), 175–195.

[17] Fletcher, A. B., and Stahler, S. W. The luminosity functions of embedded stellar clusters. 1: Method of solution and analytic results. *APJ 435* (Nov. 1994), 313–328.

[18] Frank, A., Ray, T. P., Cabrit, S., Hartigan, P., Arce, H. G., Bacciotti, F., Bally, J., Benisty, M., Eislöffel, J., Güdel, M., Lebedev, S., Nisini, B., and Raga, A. Jets and Outflows from Star to Cloud: Observations Confront Theory. In *Protostars and Planets VI* (Jan. 2014), H. Beuther, R. S. Klessen, C. P. Dullemond, and T. Henning, Eds., p. 451.

[19] Gallet, F., Zanni, C., and Amard, L. Rotational evolution of solar-type protostars during the star-disk interaction phase. *632* (Dec. 2019), A6.

[20] Gammie, C. F. Layered Accretion in T Tauri Disks. *APJ 457* (Jan. 1996), 355.

[21] Hartmann, L., and Bae, J. How do T Tauri stars accrete? *MNRAS 474* (Feb. 2018), 88–94.

[22] Hartmann, L., Calvet, N., Gullbring, E., and D'Alessio, P. Accretion and the Evolution of T Tauri Disks. *APJ 495*, 1 (Mar 1998), 385–400.

[23] Hartmann, L., Herczeg, G., and Calvet, N. Accretion onto Pre-Main-Sequence Stars. *ARAA 54* (Sept. 2016), 135–180.

[24] Hayashi, C. Structure of the Solar Nebula, Growth and Decay of Magnetic Fields and Effects of Magnetic and Turbulent Viscosities on the Nebula. *Progress of Theoretical Physics Supplement 70* (1981), 35–53.

[25] Herbst, W., Bailer-Jones, C. A. L., and Mundt, R. The Mass Dependence of Stellar Rotation in the Orion Nebula Cluster. *APJl 554* (June 2001), L197–L200.

[26] Hernández, J., Hartmann, L., Calvet, N., Jeffries, R. D., Gutermuth, R., Muzerolle, J., and Stauffer, J. A Spitzer View of Protoplanetary Disks in the γ Velorum Cluster. *APJ 686* (Oct. 2008), 1195–1208.

[27] Kenyon, S. J. Dynamical Evolution of Protoplanetary Disks. In *Tetons 4: Galactic Structure, Stars and the Interstellar Medium* (Jan. 2001), C. E. Woodward, M. D. Bicay, and J. M. Shull, Eds., vol. 231 of *Astronomical Society of the Pacific Conference Series*, p. 594.

[28] King, L. *On the direct numerical calculation of elliptic functions and integrals*. The University Press, 1924.

[29] Landau, L. D., and Lifshitz, E. M. *Fluid Mechanics*. 1987.

[30] Lin, D. N. C., and Pringle, J. E. The Formation and Initial Evolution of Protostellar Disks. *APJ 358* (Aug 1990), 515.

[31] Marov, M., and Kolesnichenko, A. Turbulence and self-organization.

[32] Mestel, L. Problems of Star Formation - I. *Quarterly Journal of the Royal Astronomical Society 6* (June 1965), 161.

[33] Mihalas, D., and Mihalas, B. *Foundations of radiation hydrodynamics*. 1984.

[34] Mihalas, D., and Mihalas, B. W. *Foundations of radiation hydrodynamics*. 1984.

[35] Mihalas, D., and Winkler, K.-H. A., Eds. *Radiation Hydrodynamics in Stars and Compact Objects* (1986), vol. 255 of *Lecture Notes in Physics, Berlin Springer Verlag*.

[36] Palla, F., and Stahler, S. W. The evolution of intermediate-mass protostars. I - Basic results. *APJ 375* (July 1991), 288–299.

[37] Pringle, J. E. Accretion discs in astrophysics. *ARAA 19* (Jan. 1981), 137–162.

[38] Ragossnig, F., Dorfi, E. A., Ratschiner, B., Gehrig, L., Steiner, D., Stoeckl, A., and Johnstone, C. 1+1D implicit disk computations. *Computer Physics Communications* (2020; in press).

[39] Ragossnig, F., Gehrig, L., Dorfi, E. A., Steiner, D., and Stökl, A. Mass limits for stationary protoplanetary accretion disks. *arXiv e-prints* (Jan. 2020, in preparation), arXiv:2001.03425.

[40] Romanova, M. M., Ustyugova, G. V., Koldoba, A. V., and Lovelace, R. V. E. Launching of conical winds and axial jets from the disc-magnetosphere boundary: axisymmetric and 3D simulations. *MNRAS 399*, 4 (Nov. 2009), 1802–1828.

[41] Shakura, N. I., and Sunyaev, R. A. Black holes in binary systems. Observational appearance. *AAP 24* (1973), 337–355.

[42] Toomre, A. On the gravitational stability of a disk of stars. *APJ 139* (May 1964), 1217–1238.

[43] Trova, A., Huré, J.-M., and Hersant, F. Self-gravity in thin discs and edge effects: an extension of Paczynski's approximation. *AAP 563* (Mar. 2014), A132.

[44] van Leer, B. Towards the ultimate conservative difference scheme. III - Upstream-centered finite-difference schemes for ideal compressible flow. IV - A new approach to numerical convection. *Journal of Computational Physics 23* (Mar. 1977), 263–299.

[45] Vorobyov, E., and Elbakyan, V. Gravitoviscous protoplanetary disks with a dust component. ii. spatial distribution and growth of dust in a clumpy disk. *Astronomy Astrophysics 631* (09 2019).

[46] Vorobyov, E. I., Skliarevskii, A. M., Elbakyan, V. G., Pavlyuchenkov, Y., Akimkin, V., and Guedel, M. Global evolution of a gravitoviscous protoplanetary disk. I. The importance of the inner sub-au region. *arXiv e-prints* (May 2019), arXiv:1905.11335.

[47] Zhang, S., and Jin, J. *Computation of Special Functions*. A Wiley-Interscience publication. Wiley, 1996.

[48] Zhu, Z., Hartmann, L., and Gammie, C. Long-term Evolution of Protostellar and Protoplanetary Disks. II. Layered Accretion with Infall. *APJ 713*, 2 (Apr. 2010), 1143–1158.